

# Strontium Substituted Tricalcium Phosphate Bone Cement: Short and Long-Term Time-Resolved Studies and In Vitro Properties

Julietta V. Rau,\* Inna V. Fadeeva, Anna A. Forsenkova, Galina A. Davydova, Marco Fosca, Yaroslav Yu. Filippov, Iulian V. Antoniac, Aurora Antoniac, Annalisa D'Arco, Marta Di Fabrizio, Massimo Petrarca, Stefano Lupi, Massimo Di Menno Di Bucchianico, Viktoriya G. Yankova, Valery I. Putlayev, and Mihai Bogdan Cristea

Due to a significant influence of strontium (Sr) on bone regeneration, Sr substituted  $\beta$ -tricalcium phosphate (Sr-TCP) cement is prepared and investigated by short- and long-term time-resolved techniques. For short-term investigations, energy-dispersive X-ray diffraction, infrared spectroscopy, and, for the first time, terahertz time-domain spectroscopy techniques are applied. For long-term time-resolved studies, angular dispersive X-ray diffraction, scanning electron microscopy, mechanical tests, and behavior in Ringer solution are carried out. After 45 min of the cement setting, the Sr-TCP phase is no longer detectable. During this time period, an appearance and constant increase of the final brushite phase are registered. The compressive strength of the Sr-TCP cement increases from 4.5 MPa after 2 h of setting and reaches maximum at 13.3 MPa after 21 d. After cement soaking for 21 d in Ringer solution, apatite final product, with an admixture of brushite and TCP phases is detected. The cytotoxicity aspects of the prepared cement are investigated using NCTC 3T3 fibroblast cell line, and the cytocompatibility—by human dental pulp mesenchymal stem cells. The obtained results allow to conclude that the developed Sr-TCP cement is promising for biomedical applications for bone tissue.

## 1. Introduction

Bone tissue diseases, such as osteomyelitis and osteoporosis, significantly reduce the quality of patients' life.<sup>[1,2]</sup> Bone tissue degradation leads to dysfunctions of the musculoskeletal system resulting in disorders also in other organ systems.<sup>[3]</sup> The consequences of bone tissue diseases and complications in their treatment pose the problem of designing new materials that could contribute to the restoration of bone tissue and could be used in a minimally invasive surgery. Bone calcium phosphate cements (CPCs) are promising solution for this problem. Currently, CPCs are widely used in dentistry<sup>[4]</sup> to restore teeth functions and remineralize tissues after caries removal.<sup>[5,6]</sup> In surgery, CPCs are used in minimally invasive treatment for filling bone defects and for drug delivery.<sup>[7–9]</sup> The choice of brushite (dicalcium phosphate

J. V. Rau, M. Fosca, M. Di Menno Di Bucchianico  
Istituto di Struttura della Materia  
Consiglio Nazionale delle Ricerche (ISM-CNR)  
Via del Fosso del Cavaliere 100, Rome 00133, Italy  
E-mail: giulietta.rau@ism.cnr.it

J. V. Rau, V. G. Yankova  
Department of Analytical  
Physical and Colloid Chemistry  
Institute of Pharmacy

I. M. Sechenov First Moscow State Medical University  
Trubetskaya 8, build. 2, Moscow 119991, Russian Federation

I. V. Fadeeva, A. A. Forsenkova  
A.A. Baikov Institute of Metallurgy and Material Science RAS  
Leninsky 49, Moscow 119334, Russian Federation

G. A. Davydova  
Institute of Theoretical and Experimental Biophysics  
Russian Academy of Sciences  
Institutskaya 3, Puschino, Moscow region 142290, Russian Federation

Y. Y. Filippov  
Department of Materials Science  
Lomonosov Moscow State University  
Building, 73, Leninskie Gory, 1, Moscow 119991, Russian Federation

Y. Y. Filippov  
Research Institute of Mechanics  
Lomonosov Moscow State University  
Michurinsky pr., 1, Moscow 119192, Russian Federation

I. V. Antoniac, A. Antoniac  
Department of Metallic Materials Science and Physical Metallurgy  
University Politehnica of Bucharest  
Street Splaiul Independentei no 313, sector 6, Bucharest 060042, Romania

A. D'Arco, S. Lupi  
INFN-LNF  
Via E. Fermi 40, Frascati 00044, Italy

A. D'Arco, S. Lupi  
Physics Department  
University of Rome 'La Sapienza'  
Piazzale Aldo Moro 5, Rome 00185, Italy

 The ORCID identification number(s) for the author(s) of this article can be found under <https://doi.org/10.1002/admi.202200803>.

© 2022 The Authors. Advanced Materials Interfaces published by Wiley-VCH GmbH. This is an open access article under the terms of the Creative Commons Attribution License, which permits use, distribution and reproduction in any medium, provided the original work is properly cited.

DOI: 10.1002/admi.202200803

dihydrate (DCPD)) or apatite cement depends on the medical requirements in each case: bioresorption rate is higher for brushite cements, while mechanical strength for apatite ones.<sup>[10–12]</sup> In particular, tuning cements' properties is possible by cationic substitutions.<sup>[13–18]</sup> In addition, the substitution ion can impart useful biological properties.<sup>[14–18]</sup>

As a key trace element contained in natural bone, strontium (Sr) can be used as a substitution ion.<sup>[19–21]</sup> Strontium ranelate has become a mainstream drug for osteoporosis treatment. Positive effects of Sr on osteoporosis and osteoarthritis were reported.<sup>[22,23]</sup> One of the important properties of Sr, causing a high interest in materials research, is its osteoinductivity. Sr has a dual effect on bone remodeling. It induces the increase in the activity of osteoblasts thus enhancing the new bone growth and, at the same time, suppresses the activity of osteoclasts and, consequently, reduces the bone resorption.<sup>[24–26]</sup> The influence of Sr on bone formation process is dose-dependent, i.e., various Sr content in materials composition has different effects on cells in vitro or surrounding tissues in vivo.<sup>[25,27]</sup> Increased adhesion and cell proliferation were found in cements modified with Sr, which depended not only on the Sr amount, but also of the processing parameters on the final performance of cements.<sup>[28–31]</sup>

Moreover, Sr is also able to stimulate angiogenesis, playing an important role in bone regeneration.<sup>[32]</sup> The incorporation of Sr in the cement structure leads to an increase in its macro and microporosity.<sup>[33,34]</sup> The microstructure of cement depends on the Sr content.<sup>[35]</sup> Partial substitution of calcium leads to a decrease in the size of brushite lamellar particles, whereas its complete substitution leads to the formation of microspheres.<sup>[35]</sup> Cements containing Ca:Sr = 1:1. have the most cell-friendly surface with the best adhesion having a finely lamellar microstructure.<sup>[35]</sup> In addition, Sr-containing calcium phosphate nanoparticles promote DNA adsorption on the surface and improve gene delivery related properties.<sup>[36]</sup>

For regenerative medicine, brushite cements are particularly interesting.<sup>[37]</sup> It was reported that Sr-substituted brushite cements stimulate the formation of bone tissue in vivo better

than Sr-substituted hydroxyapatite (HA) cements.<sup>[38,39]</sup> In the case of Sr-DCPD, there is a cumulative effect of Sr on osteogenesis and a higher rate of DCPD bioresorption compared to HA cements.<sup>[23]</sup>

As a precursor for the brushite cements preparation,  $\beta$ -tricalcium phosphate ( $\beta$ -TCP,  $\beta$ -Ca<sub>3</sub>(PO<sub>4</sub>)<sub>2</sub>) or, in this case, Sr- $\beta$ -TCP,<sup>[40]</sup> is mainly used. A number of studies were devoted to Sr-substituted brushite cements. Several groups reported phase composition, microstructure, mechanical properties, in vitro and in vivo behavior of Sr-containing brushite cements based on  $\beta$ -TCP.<sup>[41–50]</sup> The influence of Sr<sup>2+</sup> ions on the listed parameters as well as on the setting properties was reported.<sup>[41–50]</sup>

The aim of the present study was to investigate physico-chemical and biological in vitro properties of the developed Sr-TCP cement, focusing on short and long-term time-resolved investigations of cement hardening process. For this former purpose, time-resolved energy-dispersive X-ray diffraction (EDXRD) technique, IR spectroscopy, and, for the first time for CP cements investigation, terahertz time-domain spectroscopy (THz-TDS), techniques were applied. For the long-term time-resolved investigations, scanning electron microscopy (SEM) characterizations, mechanical tests, and behavior in the Ringer solution were carried out. Biological in vitro cell test studies of cements included an assessment of their possible toxicity (indirect contact of the test culture (extracts from samples)) by MTT test of the metabolic activity of a standard NCTC 3T3 fibroblast cell line of mouse subcutaneous connective tissue, and cytocompatibility (for nontoxic samples, direct contact with a cell culture) of human dental pulp mesenchymal stem (DPMSC) cells seeded on the samples surface.

## 2. Results and Discussion

In the present investigation, we performed short and long-term time-resolved studies of the hardening process of the prepared cements. The short-term studies were carried out by the EDXRD, THz-TDS, and IR techniques and regard the first 21 h of the hardening process.

### 2.1. Short Term Time-Resolved Measurements

#### 2.1.1. Ex Situ Sr-TCP Measurements

Ex situ EDXRD spectra were collected upon both the Sr-TCP and TCP pristine powder samples, in order to individuate possible differences induced by the Sr substitution.

**Figure 1** shows a comparison between the mentioned spectra. Patterns related to Sr-substituted and unsubstituted samples appear very similar. Nevertheless, the TCP pattern is characterized by better resolved peaks. Moreover, several Bragg reflections of TCP pattern show a slight but still detectable higher relative intensity, if compared to the Sr-TCP one. Those dissimilarities can be attributed to a possible lower crystallinity degree, induced by the Sr substitution. Finally, the anisotropic Sr K<sub>α</sub> and K<sub>β</sub> fluorescence signals are well detectable for the Sr-TCP powder sample.

M. Di Fabrizio  
Laboratory of Biological Electron Microscopy  
IPHYS  
SB  
EPFL & Department of Fundamental Microbiology  
Faculty of Biology and Medicine  
UNIL  
Lausanne CH-1015, Switzerland

M. Petrarca  
SBAl-Department of Basic and Applied Sciences for Engineering  
Physics University of Rome 'La Sapienza'  
Via Scarpa 16, Rome 00161, Italy  
M. Petrarca  
INFN-Section of Rome "La Sapienza"  
P.le Aldo Moro 2, Rome 00185, Italy

V. I. Putlayev  
Chemistry Department  
M.I. Lomonosov Moscow State University  
GSP-1, 1–3 Leninskiye Gory, Moscow 119991, Russian Federation  
M. B. Cristea  
Department of Morphological Sciences  
Carol Davila University of Medicine and Pharmacy  
37 Dionisie Lupu Str., District 2, Bucharest 020021, Romania

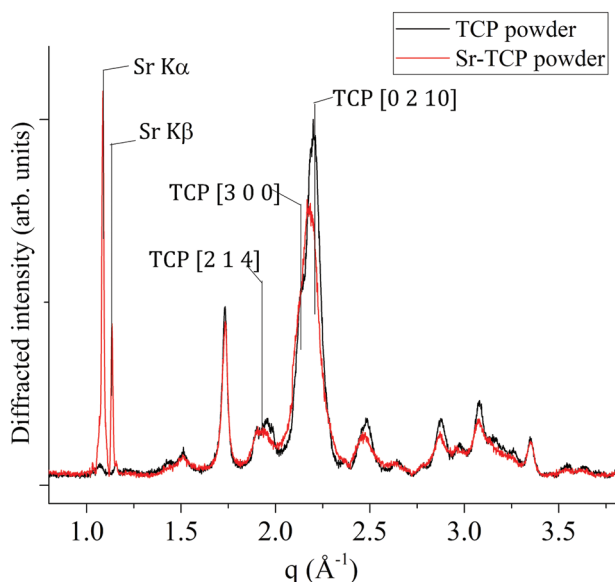


**Figure 1.** Comparison between EDXRD patterns collected upon pristine powders of TCP (black line) and Sr-TCP (red line). Most intense Bragg reflections, along with Sr  $K_{\alpha}$  and  $K_{\beta}$  fluorescence signals (Sr-TCP), were labeled.

The EDXRD technique was previously applied to study the hardening mechanism of the calcium phosphate-based cements.<sup>[14,15,17,51,52]</sup> **Figure 2** depicts a comparison of the first and last EDXRD patterns collected on the Sr-TCP cement after 1 min (black line) and 21 h (red line) of processing, respectively. Qualitative analysis reveals significant differences between the 1 min pattern (starting of the cement hardening process) and the 21 h one (end of process). Initial phase was constituted by Sr-TCP, identified by main reflections present in 1 min pattern (black pattern in Figure 2) at positions of  $q = 2.18 \text{ (}\text{\AA}^{-1}\text{)}$ ,  $q = 2.10 \text{ (}\text{\AA}^{-1}\text{)}$  and  $q = 1.97 \text{ (}\text{\AA}^{-1}\text{)}$ , respectively, attributed to reflections labeled with [0 2 10] [3 0 0] and [2 1 4] Miller indexes, by comparison with literature data [PCPDF 09-0169]. Moreover, intense signals generated from Sr  $K_{\alpha}$  and  $K_{\beta}$  fluorescence were visible in both

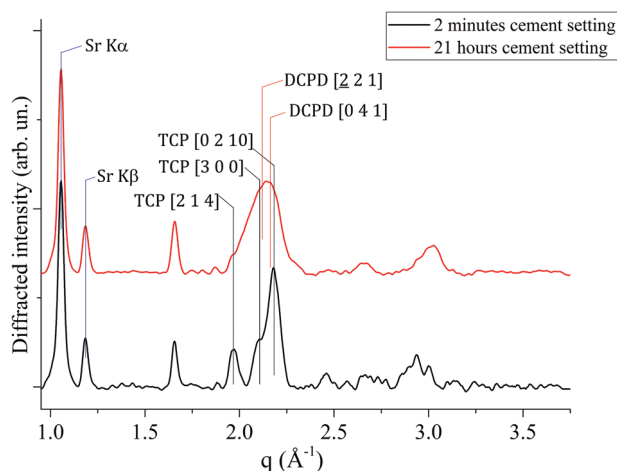


**Figure 2.** Comparison between EDXRD patterns collected during the initial stage (2 min—black line) and the final stage (21 h—red line) of the hardening process of Sr-TCP cement. Reported  $q$  range ( $1 \div 4 \text{ (}\text{\AA}^{-1}\text{)}$ ) was chosen to highlight the region with peaks of interest.

the patterns and testified to the presence of Sr in the cement. In the 21 h spectrum (red pattern in Figure 2), representative of the final stage of cement hardening process, TCP peaks with significantly decreased intensities were detected. New reflections appeared at positions of  $q = 2.16 \text{ (}\text{\AA}^{-1}\text{)}$  and  $q = 2.10 \text{ (}\text{\AA}^{-1}\text{)}$  in a convoluted signal. We were able to assign Miller indexes to all of these peaks after an accurate attribution of the new reflections, and the new phase was recognized as brushite (DCPD) [PCPDF 09-0077]. DCPD (0 4 1) 75% R.I., DCPD (2 2 1) (50% R.I.) (where R.I. stands for relative intensity) reflections allowed us to infer that Sr-TCP phase undergoes almost total conversion to DCPD phase. Traces of unconverted TCP were detectable as the shoulder of the peak at  $q = 1.97 \text{ (}\text{\AA}^{-1}\text{)}$ .

The real-time monitoring of the Sr-TCP cement was conducted by the EDXRD technique by collecting a diffraction pattern every 2 min. In **Figure 3A,B**, a 3D perspective of a sequence of spectra collected during 21 h of hardening process, are reported. Both panels show the same sequence of patterns, at

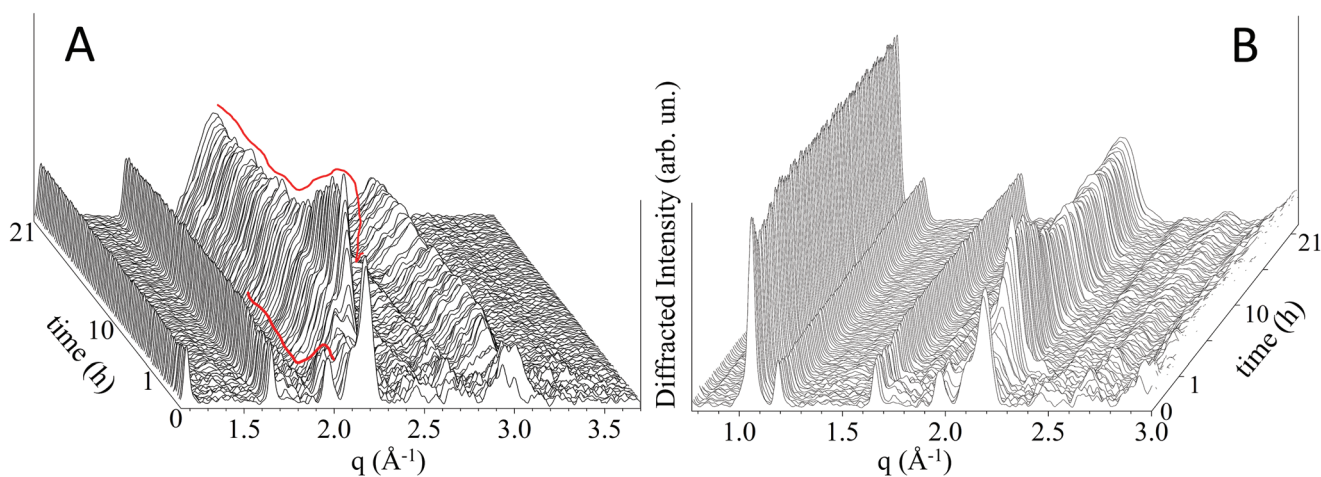


**Figure 3.** A,B) 3D perspectives at a different view angle of sequence of all patterns collected during the EDXRD real-time monitoring of Sr-TCP cement hardening upon 21 h. In panel A, time evolution of TCP [2 1 4] and DCPD [2 2 1] and [0 4 1] reflections can be easily followed, while time evolution of reflections TCP [0 2 10] and [3 0 0] is better visible in 3D sequence reported in panel B.

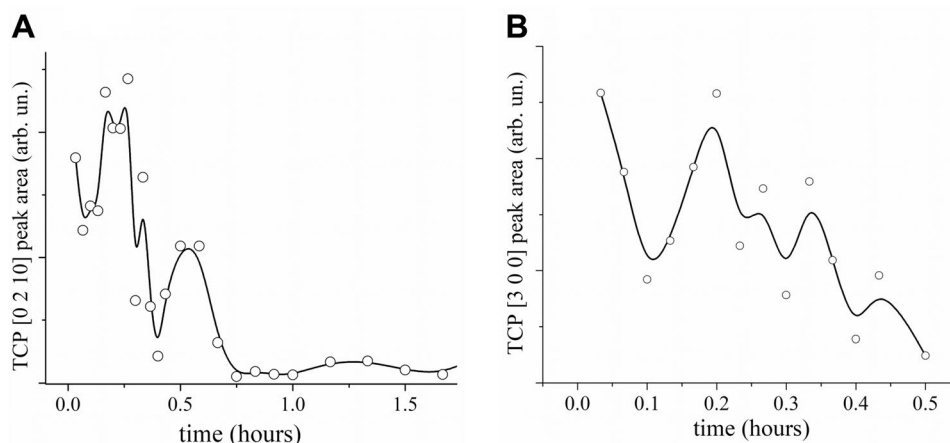


**Figure 4.** Time evolution of A) TCP [0 2 10] and B) [2 1 4] reflections during the first stage of cement setting process. Periodic modulation of intensity characterized both peaks until their disappearance occurred after about 30 ± 40 min.

different perspective view, in order to highlight the time evolution of peaks of interest. From the qualitative point of view, it is possible to confirm that no intermediate phases were detected for the whole duration of monitoring. It is possible to confirm also that the important variation of the signal intensity is the product of a complex modulation, involving in different ways of all the phases. The Sr-TCP peak intensity undergoes a fast and periodic decrease and increase during the first hour. Within 1.5 h from the beginning of the process, the Sr-TCP peak intensity decreased close to zero. At  $t = 3$  h, new reflections appeared and their intensity constantly increased. After an accurate attribution, the new phase was identified as DCPD (brushite), and new reflections, labeled as  $\text{CaHPO}_4 \cdot 2\text{H}_2\text{O}$ , DCPD (0 4 1) 75% R.I.) and (2 2 1) (50% R.I.), testified almost total conversion of the TCP phase into the DCPD.

In order to precisely describe cement transformations as a function of time, quantitative analysis was performed on peaks present in the range of  $q = 1.8 \pm 2.3(\text{\AA}^{-1})$ . This region was identified as one of the most representative to observe structural changing taking place upon hardening process. Gaussian fitting model was used to extrapolate peaks' characteristics. Quantitative analysis was performed on every spectrum registered during the real-time monitoring in the region of interest.

The time dependence of the intensity of peaks (peak area) TCP [2 0 10] and [3 0 0] is reported in **Figure 4A,B**, respectively. Strong, periodic, and relatively fast intensity modulation of both reflections can be observed during the first 30–40 min of the cement hardening. Each modulation is characterized by a periodic alternation of local maxima and minima. After several such periods, intensities definitively decrease down to values close to zero. These phenomena could be related to the fast dissolution/desegregation of TCP powder grains into finer particles and their subsequent aggregation. During this stage, part of TCP dissolves within the liquid matrix and precipitate as the DCPD phase. For both reflections, this phenomenon is characterized by similar time scale and definitively terminates after 30–40 min.

Quantitative analysis on the region of interest allowed us to follow in real time the appearance a new diffraction signal, constituted by convolution of two reflections at positions  $q = 2.16$

and  $2.10(\text{\AA}^{-1})$ . Time evolution of these new reflections is shown in **Figure 5**. These reflections were attributed to the DCPD phase (DCPD (0 4 1) and (2 2 1)) appearing after about 2 h from the beginning of cement hardening. Their intensities increase constantly until a plateau is reached after 6 h from the beginning of the experiment. During the plateau stage, peak intensities undergo a periodic modulation. The magnitude of this modulation tends to damp over time, and it could be probably associated to a progressive settlement of the new phase (DCPD) in a definitive lattice conformation.

To our knowledge, this is the first study providing THz-TDS characterization of a calcium phosphate cement hardening process. The temporal dynamics of the Sr-TCP cement hardening was studied by performing 50 subsequent time-resolved THz-TDS measurements of the electric waveforms, covering the temporal interval of 3 h. In **Figure 6A**, a 3D plot in time-domain illustrates the evolution of the THz transmitted electric fields through the Sr-TCP cement detected at the beginning and at the end (3 h) of the process. As can be observed, some

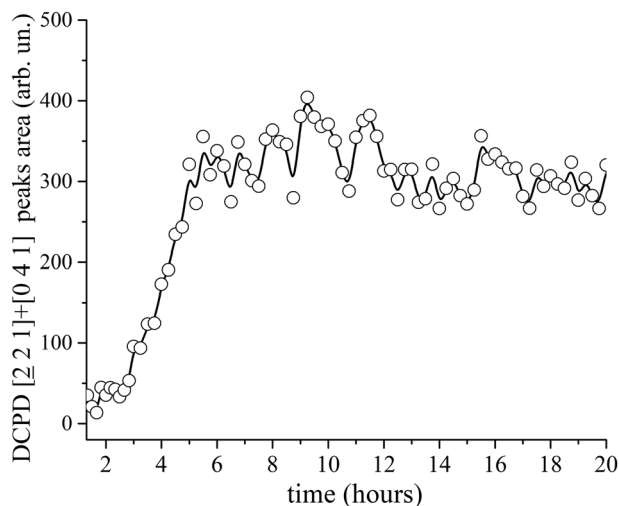


**Figure 5.** Time evolution of convoluted intensities of DCPD [2 2 1] and [0 4 1] reflections.

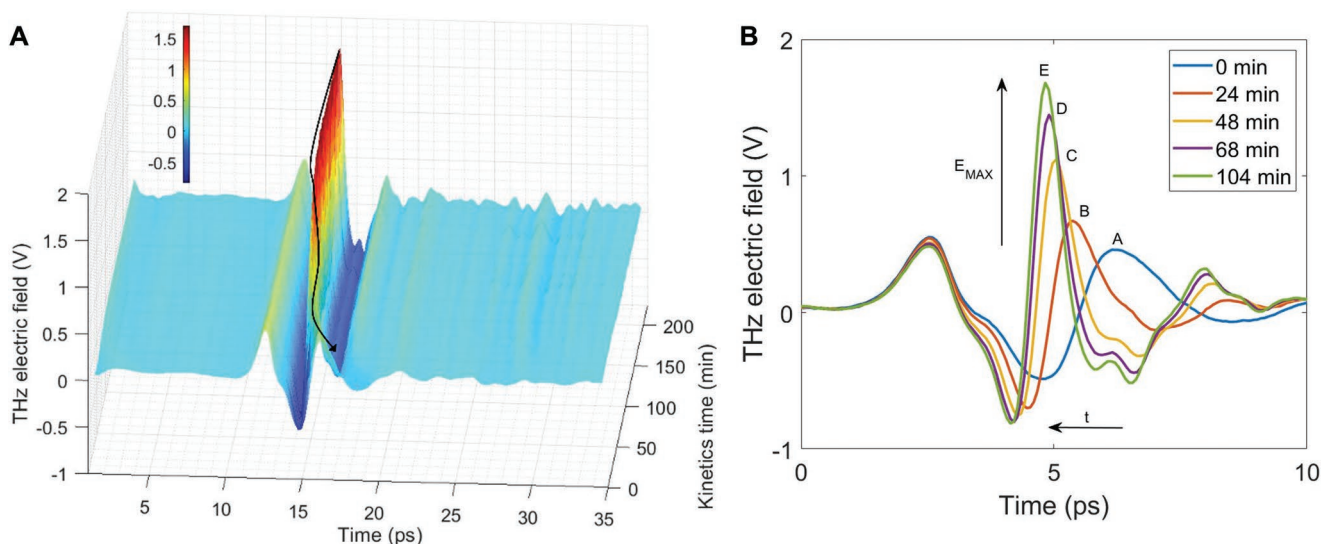


**Figure 6.** A) 3D mapping of temporal evolution of THz transmitted electric field through the Sr-TCP collected during the THz-TDS real-time monitoring of cement hardening process upon 3 h. The arrow indicates the evolution of the maximal amplitude position of THz transmitted waveform. B) Selected THz transmitted electric fields collected over 104 min from the start of the component mixing at time 0, 24, 48, 68, 104 min. Two arrows indicate the evolution of the THz pulse amplitude and the maximal amplitude position of THz transmitted waveform with an experiment time.

differences are present: the temporal evolution the maximal amplitude of THz waveform transmitted through the cement and its peak position (black arrow in Figure 6).

For simplicity in the evolution trend visualization, only selected five measurements of the THz transmitted electric field were reported in Figure 6B, specifically at times 0, 24, 48, 68, and 104 min. Each electric field was labeled on the THz main peaks with letters A, B, C, D, E, respectively. The profile of the THz transmitted electric waveform varies as a function of kinetics time. Figure 6B clearly shows that the THz signal magnitude (labeled with A–E) arises as a function of experiment time, due to the progressive reaction of components, till the complete hardening of the cement and the equilibrium conditions is searched. It reaches a maximum amplitude value  $E_{MAX}$  after 104 min. Meanwhile, the temporal evolution of maximal amplitude position of the THz electric field, is gradually shifting backwards (from 6.1 ps to 4.8 ps in Figure 6B). The time-dependent changes in the maximal THz amplitude and temporal evolutions of its position are attributed to the hardening process. In this process, the THz amplitude variation ( $A < \dots < E$ ) is directly linked to the gradual loss of water, to which THz radiation is very sensitive,<sup>[54]</sup> and the THz shape is linked to the formation of a new compound from the initial mixing. In order to estimate the transformation time of evolving hardening process, a quantitative analysis was performed on the intensity of the THz transmitted waveform.

In **Figure 7**, the intensities of THz pulses for all the 50 measurements were plotted as a function of kinetics time. The THz electric field amplitude smoothly increases until reaching a maximum value  $E_{MAX}$ , defining a plateau region, and exhibiting a typical sigmoidal growth. A sigmoidal fitting was performed according to Equation (1).

$$\gamma(x) = \frac{A}{1 + e^{-C(x-x_0)}} + B \quad (1)$$

and the fit parameters are reported in **Table 1**.

A similar trend was found for the evolution of the temporal position of the maximal THz amplitude over 3 h (data not shown). The characteristic time of the chemical reaction was estimated to be 43 min.

For kinetic investigation in the IR spectral region, we performed 50 subsequent time-resolved ATR measurements starting from immediately after the mixing of cement components until spectral changes were no longer observed (240 min from it). As it can be observed, some differences are present. For simplicity in the discussion, in **Figure 8**, selected ATR

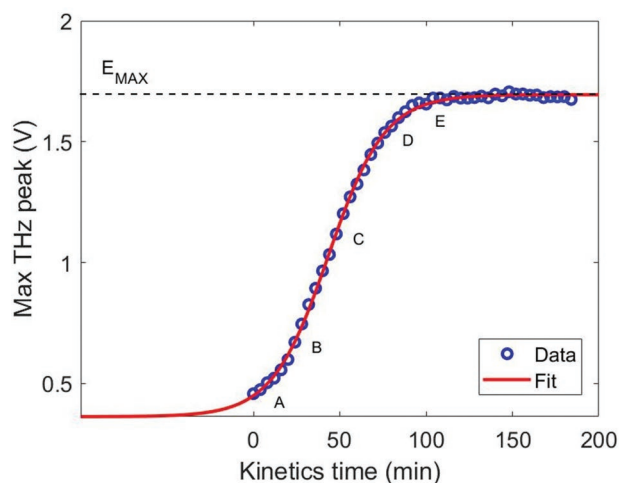


**Figure 7.** The evolution of the THz pulse amplitude with an experiment time. In blue: THz amplitude values extracted from each relative THz electric field collected during the hardening process of the cement in the temporal interval of 200 min. In red: fitting curve using Equation (1). Labels A, B, C, D, E refer to the selected THz peaks shown in Figure 6b, at times 0, 24, 48, 68 and 104 min. The dashed line indicates the plateau value  $E_{MAX}$ .

**Table 1.** Fit parameters for sigmoidal growth reported in Figure 7 and Equation (1).

A [V]	B [V]	C [min <sup>-1</sup> ]	x <sub>0</sub> [min]
1.3	0.36	0.061	43

absorption spectra were reported over 220 min from the start of cement mixing at times 0, 9, 45, 220 min. It clearly showed visible differences in the ATR absorbance as kinetics time increases, from blue to purple lines in Figure 8. All the typical peaks, associated with brushite formation, in complete agreement with the literature,<sup>[53–55]</sup> progressively appeared with the hardening process around 1000 cm<sup>-1</sup>, specifically at 986, 1064 cm<sup>-1</sup> due to the PO stretching mode. A peak at 870 cm<sup>-1</sup> associated with the POH group stretching mode started to be detectable from the first measurement (blue line in Figure 8) and appeared more defined 10 min after the mixing preparation. The bending modes, relative to O–H bond were also detected as wideband around 1205 and 1644 cm<sup>-1</sup> due to the presence of water in the base formulation. These bands became sharper as a function of kinetics time (from blue to purple). At higher wavenumbers (3000–3600 cm<sup>-1</sup>), the blue curve, the first measurement, clearly showed the broadband associated with the OH stretching. Moving towards the purple absorbance spectrum, two peaks, due to the O–H vibration stretching, appeared as doublets around 3160, 3275 cm<sup>-1</sup> and 3480, 3538 cm<sup>-1</sup>, respectively. The latter was initially detected 9 min after the mixing (red spectrum in Figure 8). During the chemical reaction, the brushite starts to form from the very early stages, and the last spectrum (recorded after 220 min) showed that the brushite formation was complete, since all the typical peaks associated with it were clearly visible. In order to estimate the temporal evolution characteristics of the hardening process, a weighted linear combination of the ATR-IR absorption spectra of pure constituents (ABS<sub>Na-cit</sub>, ABS<sub>MCPM</sub>, ABS<sub>Sr-TCP</sub>) was computed as follows (Equation 2):

$$ABS_{\text{cement}} = x_1 ABS_{\text{Na-cit}} + x_2 ABS_{\text{MCPM}} + x_3 ABS_{\text{Sr-TCP}} + x_4 ABS_{\text{brushite}} \quad (2)$$

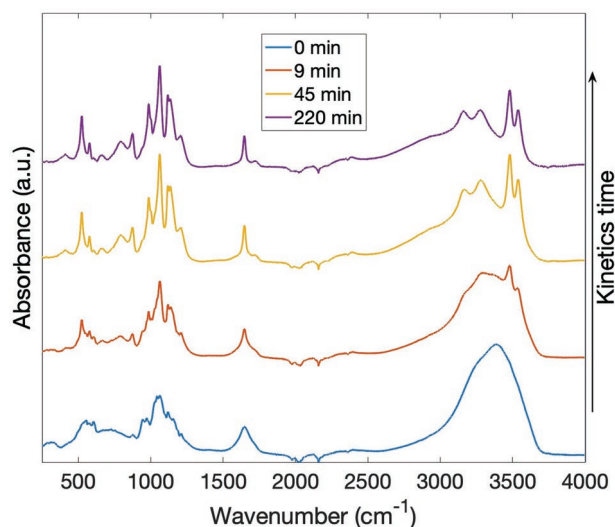


**Figure 8.** ATR absorbances of cement over 220 min as a function of wavenumber, at different measurement times as reported in the legend.

**Table 2.** Values of linear combination parameters and residual *R* calculated to estimate the goodness of the linear combination.

Kinetics time [min]	x <sub>1</sub>	x <sub>2</sub>	x <sub>3</sub>	x <sub>4</sub>	Residual <i>R</i>
0	0.75	0.17	0.51	0.31	6.0 × 10 <sup>-1</sup>
9	0.47	0.064	0.24	0.67	3.8 × 10 <sup>-1</sup>
45	0.17	0.026	0.036	0.93	1.1 × 10 <sup>-1</sup>
220	10 <sup>-10</sup>	10 <sup>-10</sup>	10 <sup>-10</sup>	1.0	1.0 × 10 <sup>-10</sup>

where x<sub>1</sub>, x<sub>2</sub>, x<sub>3</sub>, and x<sub>4</sub> represent the coefficient of the linear combination, that better reproduce the data. The fourth term (x<sub>4</sub> · ABS<sub>Brushite</sub>) was added since during the hardening process a new product (brushite) is progressively forming. Therefore, during the transition phase from the initial state (only three components) to the final state (only brushite), the measured cement spectra are not just the sum of the three constituents, but the fraction of increasing brushite contributes to it. The values of x<sub>1</sub>, x<sub>2</sub>, x<sub>3</sub>, and x<sub>4</sub> are listed in Table 2 for four selected kinetics times. The x<sub>1</sub>, x<sub>2</sub>, and x<sub>3</sub> progressively decrease reaching 0 at the end of the hardening process, meaning that all the components have converted into brushite. Conversely the x<sub>4</sub> increases as a function of kinetics time.

In Figure 9, the comparison between experimental data (blue) and linear combination (orange) of pure constituents was reported for four absorbance spectra at 0, 9, 45, and 220 min. The goodness of the linear combination was estimated, for all the four panels in Figure 6A, by the residual *R* defined as (Equation 3)

$$R = \sum (\text{Data} - \text{Lincomb})^2 \quad (3)$$

The less the residual, the better the linear combination. The values are reported in Table 2.

The insights regarding the hardening mechanisms of the Sr-TCP cement can be formulated starting from the results provided by the short-term characterizations carried out by time-resolved techniques, such as the EDXRD, THz-TDS, and IR spectroscopy. The EDXRD allowed us to characterize the early stage (first hours) of cement hardening by sampling the cement paste with intervals of minutes. This fine sampling allowed us to define the kinetic profile of the setting reaction and, the most important, to furnish some highlights of possible inherent mechanisms when trying to establish correlation between results obtained by different techniques.

Figure 4 shows time evolution of the TCP phase during the first 90 min (roughly) of the hardening process, by the real-time monitoring of the TCP Bragg reflection intensities ([0 2 10] and [3 0 0]). Fast intensities modulation characterized this stage of the process. First local minimum of kinetic profiles at reaction time *t* = 10 min (around 0.15 h) testifies the partial dissolution/disaggregation of the TCP particles into smaller ones. This first observation can be easily correlated with the IR results. Figure 8 shows the ATR absorbance collected upon cement at different time points during the first 220 min (about 4 h) of the hardening process. The ATR spectrum collected at time-point *t* = 9 min shows the first appearance of bands related to the POH and O–H group vibrations associated to the formation of brushite. Therefore, during the first 10 min of reaction,

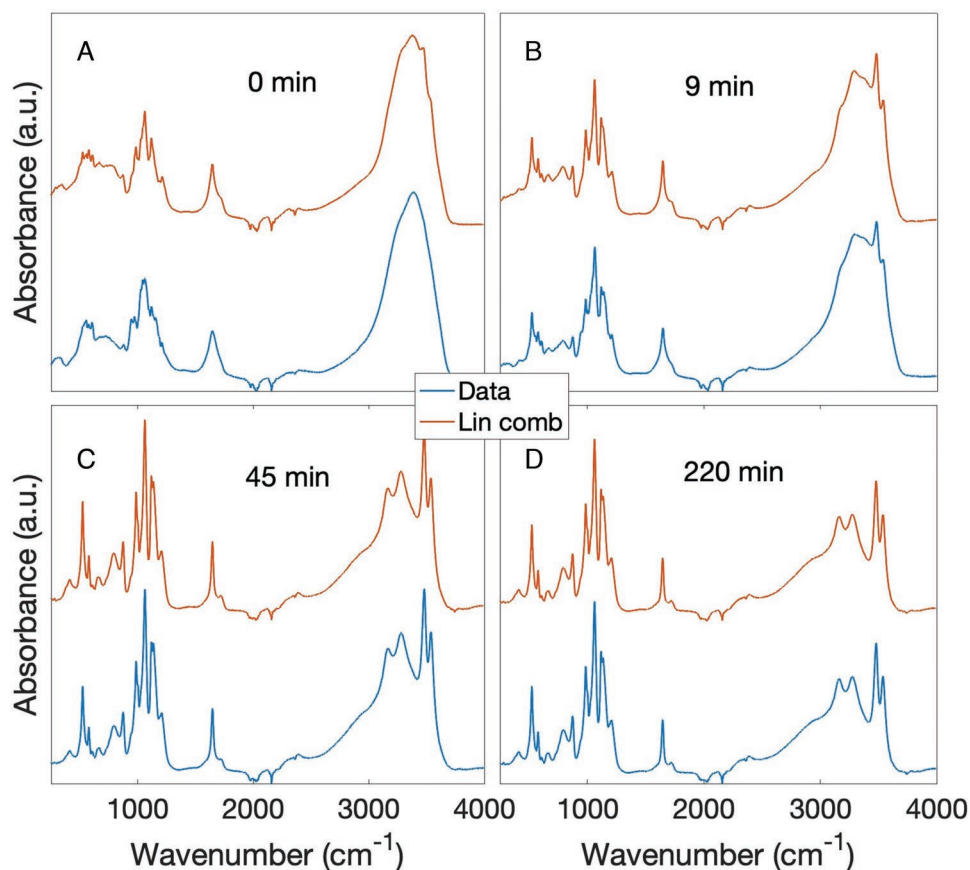


**Figure 9.** ATR absorbances of cement over 220 min as a function of wavenumber at different measurement times: A) 0 min, B) 9 min, C) 45 min and D) 220 min. In each figure, in blue—data, in red—linear combination following Equation (3).

partial dissolution/disaggregation of the TCP particles takes place. An aliquot of these particles is converted and precipitates as brushite, giving rise to the early brushite phase nucleation, while the remaining part of the TCP reaggregates in crystals.

The TCP phase modifications observed in time interval between  $t = 10$  and 40 min are characterized by a damped intensity modulation of the Bragg reflections, as reported in Figure 4. The THz-TDS spectra collected in time interval comprised between  $0 \div 104$  min (Figure 6A) show the THz electric field intensity monotone modulation and shift position that can be attributed to the formation of a new phase (brushite). Quantitative analysis carried out on THz-TDS patterns allowed us to extrapolate the max peak values and to reconstruct a time-dependent curve reported in Figure 7. Resulting time profile is characterized by a constant increase of max values that are correlated with a constant increase in formation of brushite phase. Correlating the results of the EDXRD and THz-TDS techniques is it possible to infer that during the first time interval ( $0 \div 40$  min), the hardening process can be described as a continuous dissolution/disaggregation-precipitation-nucleation process<sup>[56,57]</sup> giving rise to a constant brushite particles formation. After each modulation (as depicted in Figure 4), a part of the dissolved TCP undergoes a conversion into brushite phase (nucleation), while the remaining unreacted particles reaggregate as the TCP crystallites. The dumping of local maximum testifies the constant precipitation and conversion of the TCP

into brushite phase, constantly increasing, according to the THz-TDS results (Figure 7).

At reaction time around  $t = 45$  min, the TCP phase can be considered almost completely dissolved/disaggregated. The TCP Bragg reflections are barely detectable after reaction time  $t = 30\text{--}40$  min. On the other hand, THz-TDS sigmoidal fitting of kinetic profile (Figure 7) returns to a characteristic time of 43 min, attributable to the maximum conversion rate of the dissolved TCP into the brushite phase. Moreover, the IR spectrum collected at reaction time  $t = 45$  min shows well-defined absorbance bands of the HOP and O–H vibrational modes, representing a further confirmation of the presence of brushite phase. It can be hypothesized that at time  $t = 45$  min TCP is no longer present in crystalline form but completely dissolved and available to precipitate as DCPD. The characteristic time of 43 min, obtained by the quantitative analysis of the THz study corresponds to the maximum conversion rate point, which is in good agreement with the EDXRD results.

The conversion of the TCP into brushite takes place until the time point around  $t = 120$  min ( $t = 2$  h) when max THz-TDS peak values reach the plateau of the sigmoidal curve (Figure 7). Simultaneously, brushite phase can be observed by the real-time EDXRD monitoring as shown in Figure 5, which reports time evolution of the  $[2\ 2\ 1]$  peak intensity of brushite. It can be hypothesized that concomitantly to the final stage of conversion of the TCP and brushite nucleation, process of brushite

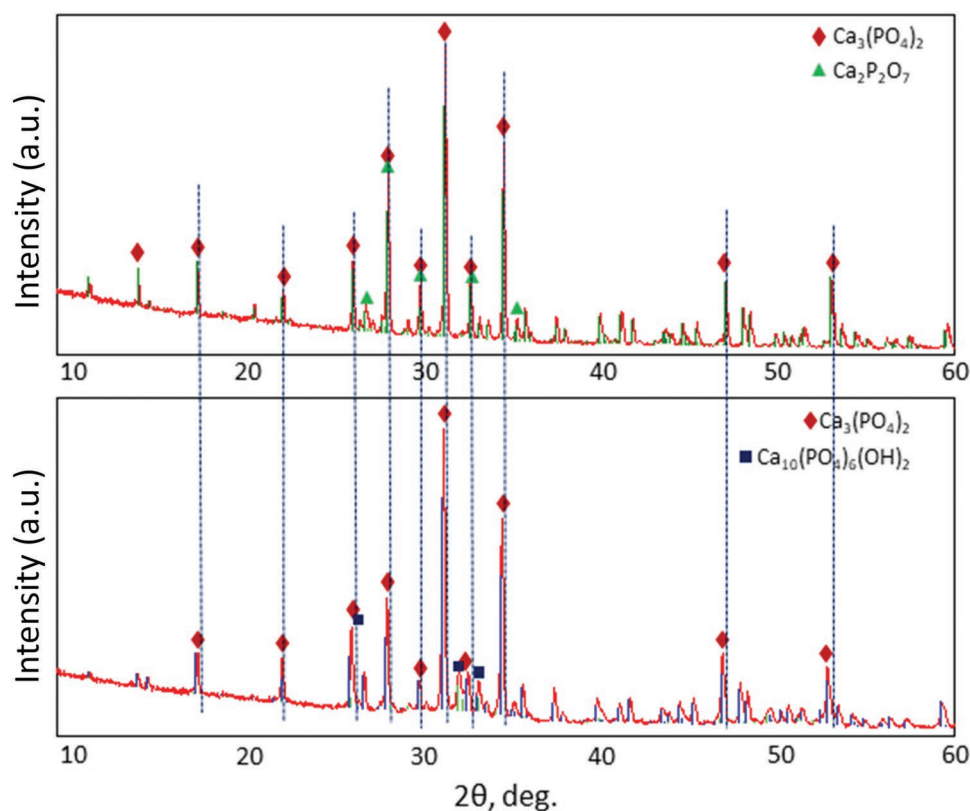


**Figure 10.** XRD patterns of  $\beta$ -TCP (upper part) and Sr- $\beta$ -TCP (lower part) powders.

crystallization takes place, where particles of brushite constantly grow into larger crystallites. This process was monitored in real time by the EDXRD technique and quantitative analysis reported in Figure 5 shows a sigmoidal growth for a duration of about 5–6 h, after that a plateau is reached and brushite primary crystallization process can be considered concluded. Afterward, in the time interval  $t = 6 \div 20$  h, only minor structural adjustments take place as observable by the fine intensity modulation of the [2 2 1] Bragg reflection. Nonlinear oscillatory behavior of calcium phosphate cements was already observed and described in our previous work.<sup>[56]</sup>

The IR pattern collected at reaction time  $t = 220$  min (about 4 h) looks very similar to the one collected at  $t = 45$  min. This result can be interpreted as a further confirmation that, during this time lapse, no further relevant conversion of the TCP into brushite phase took place and primary crystallization of the cement represented the predominant process.

The long-term time-resolved studies performed on the investigated Sr-TCP and  $\beta$ -TCP cements include XRD, SEM, mechanical strength measurements and the behavior of cements in the Ringer solution. These investigations include 1, 2, 3, 7, and 21 day time points.

## 2.2. Long-Term Time-Resolved Measurements

The phase composition of  $\beta$ -TCP and Sr-TCP powders after heat treatment at 900 °C was represented by the whitlockite (Figure 10). A calcium pyrophosphate phase (about 5 wt%) was

present in the TCP sample (Figure 10, upper part). During the TCP synthesis, areas with a Ca/P = 1 ratio were locally formed in the volume of the reaction mixture, which led to the formation of a certain amount of brushite. During further heat treatment, the brushite decomposed with the removal of water, and pyrophosphate was formed. A small amount of apatite phase was present in the Sr-TCP powder sample (Figure 10, lower figure).

In Figure 10, the XRD peaks shift to the region of smaller angles and their intensity decrease can be observed, which likely means that Sr was included in the  $\beta$ -TCP lattice, causing a distortion.<sup>[25,58]</sup> The reason for this is the larger radius of the Sr ion compared to the radius of the Ca ion (1.13 and 0.96, respectively).<sup>[59,60]</sup> However, it is impossible to draw an unambiguous conclusion based on the diffractograms.

Interestingly, that Sr occupies strictly defined positions in the lattice.<sup>[31,36]</sup> First of all, it occupies the Ca(4), and then, as its content increases and all of Ca(4) are occupied, Sr occupies Ca(1), Ca(2), Ca(3). The Ca(5) site is never occupied by Sr.<sup>[40]</sup> For comparison,  $\text{Zn}^{2+}$  (ionic radius 0.83 Å) predominantly occupies the Ca(5), without preference to the Ca(4)<sup>[40,61]</sup> In the case of substitution in brushite lattice, Sr is not limited to specific positions, occupying all free sites, which leads to an increase in the lattice volume.<sup>[30,41]</sup>

The XRD patterns of  $\beta$ -TCP and Sr- $\beta$ -TCP cements after 1, 2, 3, 7, and 21 d of hardening are shown in Figure 11A,B, respectively. The diffraction pattern of  $\beta$ -TCP cement (Figure 11A) accounts for the formation of brushite as a result of cement setting. After 1 d, the pronounced peaks were observed, related

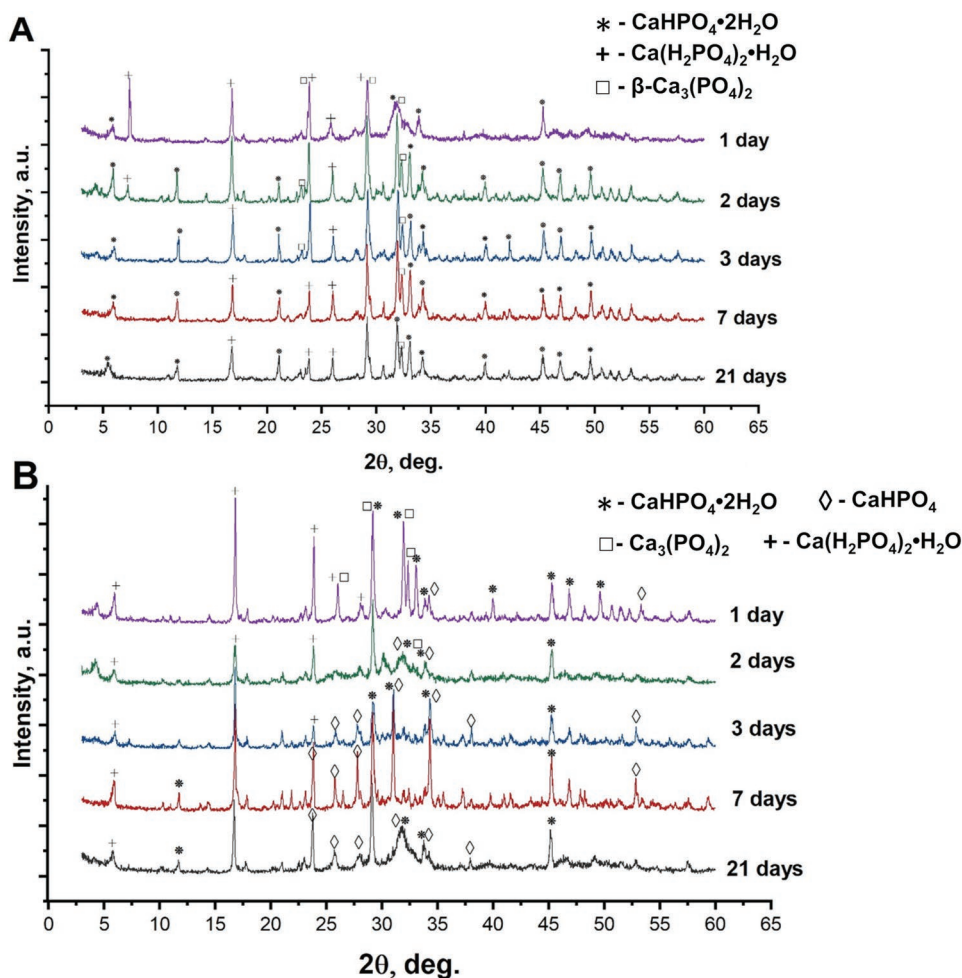


**Figure 11.** XRD patterns of A)  $\beta$ -TCP and B) Sr- $\beta$ -TCP cements after 1, 2, 3, 7, and 21 d of setting.

to the unreacted  $\beta$ -TCP and monocalcium phosphate monohydrate (MCPM). Starting from the second day, the intensity of the reagent peaks decreased and peaks characteristic of the brushite structure appeared and kept constant until the end (21 d).

The X-ray patterns of the Sr-TCP cement look differently (Figure 11B). After 1 d, the pronounced peaks of unreacted  $\beta$ -TCP and MCPM, brushite peaks, and monetite (dicalcium phosphate anhydrous (DCPA,  $\text{CaHPO}_4$ )) low-intensity peaks were observed. After 2 d, the intensity of almost all peaks decreased, and peaks broadening was observed in the  $2\theta = 25\text{--}35$  region. After 3 d, peaks characteristic for monetite and brushite were clearly visible in the diffraction pattern. After 7 days, the effect of peaks sharpening was detected, whereas after 21 d, broad peaks with lower intensity appeared again. As a final result, the Sr-TCP cement transformed into monetite and brushite, this transformation process was accompanied by a crystallinity decrease. It can be hypothesized that this oscillating behavior of the cement is similar to a phenomenon described in refs. [56, 62]. In that study, a similar oscillating behavior was observed for the Zn-doped whitlockite cement, which transformed into brushite and scholzite, and for the HA cement exhibiting oscillations in crystallinity until the endpoint

of the setting reaction. It can be also supposed that the oscillating effect is enhanced by the Sr incorporation in the calcium phosphate crystal lattice.<sup>[63]</sup>

As to the monetite presence in the Sr-TCP cement, Alkhraisat et al. also observed that the set Sr-TCP cement consisted mainly of brushite and monetite.<sup>[41–43]</sup> Moreover, with the increase in Sr content, the content of the monetite phase increased.<sup>[42,43,46]</sup>

The Sr ion introduction in the  $\beta$ -TCP affected the microstructure. On Figure 12A1, the typical characteristic morphology of TCP can be observed, whereas on Figure 12A2, for Sr-TCP cement, the densely packed lamellar crystals of brushite phase can be seen. This last observation is in agreement with the results obtained by the EDXRD, THz-TDS, and IR spectroscopy techniques, which detected the transformation of Sr-TCP into brushite at 45 min time point. Overall, the microstructure of the Sr-TCP cement is more homogeneous, compared with cement from unsubstituted TCP (see Figure 12, panels B1–B2, C1–C2, and D1–D2). The obtained results are similar to the results reported by Taha in the ref. [46], which investigated Sr-TCP cement and observed a similar morphology. Also, in that case, the particles did not have a specific orientation.

Simultaneously with the change in the phase composition, the compressive strength of cements increased from 3.1 and

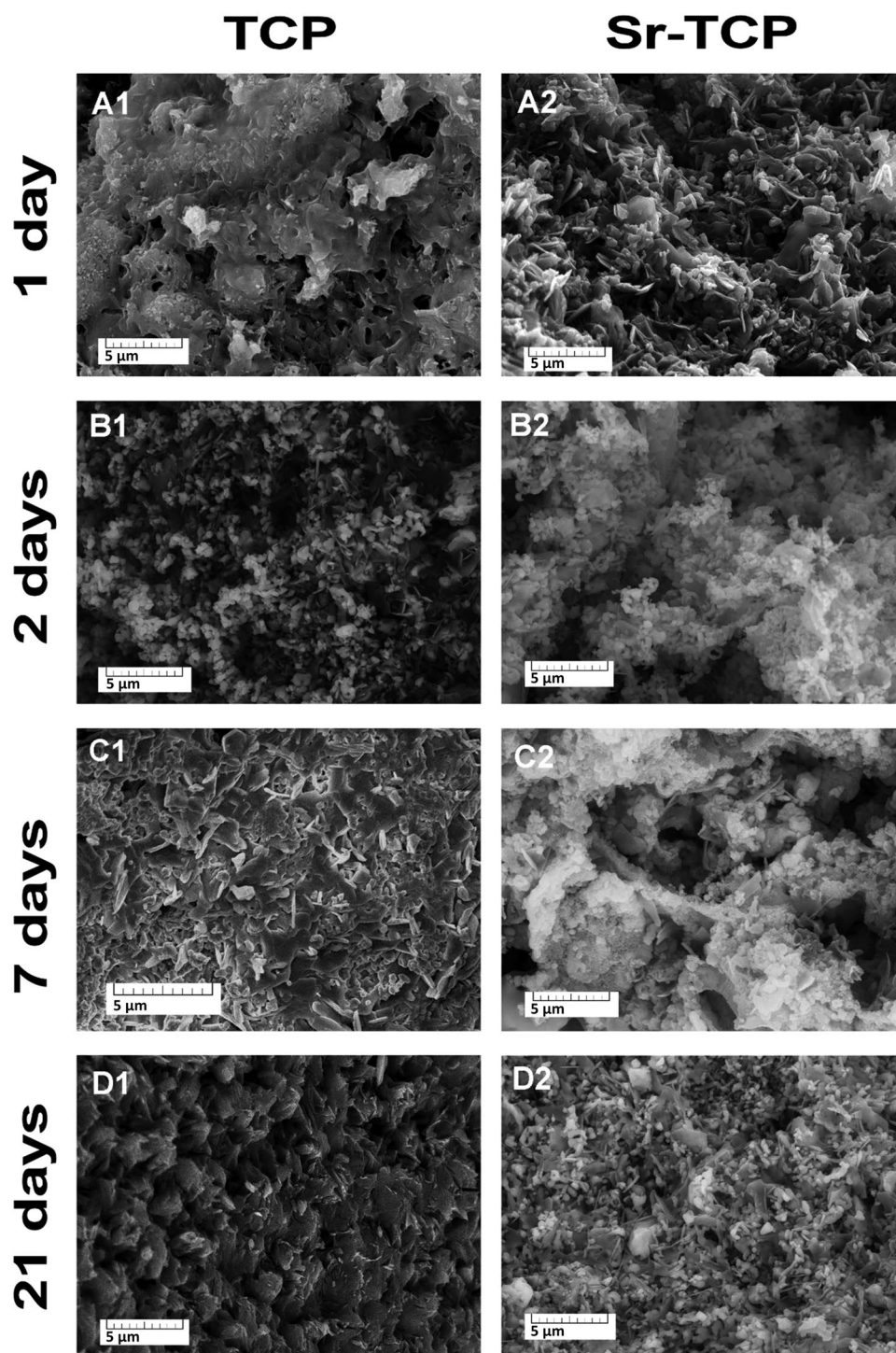


**Figure 12.** SEM image of the microstructure of TCP and Sr-TCP cements at different hardening time.

4.5 MPa (Figure 13, TCP and Sr-TCP, respectively) after 2 h of setting, to 8.7 and 9.6 MPa (TCP and Sr-TCP, respectively) after 7 d. The compressive strength reached its maximum value, 11.9 and 13.3 MPa (TCP and Sr-TCP, respectively) after 21 d (Figure 13). Somewhat higher strength of the Sr-TCP cement already after 2 h of hardening can be explained by the early formation of the brushite (see characteristic morphology

in Figure 12A2), while TCP cement still had a heterogeneous morphology (Figure 12A1) and, accordingly, a lower strength (Figure 13). However, due to a large standard deviation of the obtained compressive strength values, it is difficult to draw an unambiguous conclusion about the increased mechanical strength of the Sr-substituted cement compared to the cement without Sr.

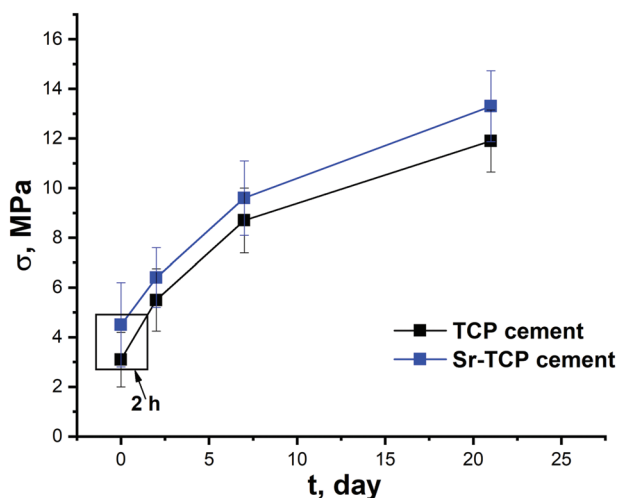


**Figure 13.** Time dependence of mechanical strength of TCP and Sr-TCP cements.

In the literature,<sup>[49]</sup> an increase in the strength of Sr-substituted calcium phosphate cements was reported. Indeed, the strength of Sr-TCP cement, composed of a mixture of  $\alpha$ -TCP and brushite phases (phase ratio of 3.4:1) was close to the strength of human spongy bone (24 MPa). The same dependence was observed for apatite cements. The value of the compressive strength of the Sr-HA/Sr-TCP cement with a phase ratio of 75:25 wt% was  $9.2 \pm 1.3$  MPa.<sup>[33]</sup> This is approximately twice of the strength of the same cement without Sr ( $4.6 \pm 0.9$  MPa).<sup>[33]</sup> However, the strength of Sr-CDHA (calcium deficient HA) cement formed as a result of hydrolysis of  $\alpha$ -TCP was lower than CDHA without Sr (9 and >20 MPa, respectively).<sup>[27]</sup>

The  $\beta$ -TCP and Sr-TCP cements were soaked in the Ringer solution for 21 d. The phase composition and microstructure of cements transformation upon soaking of cements in the Ringer

solution are presented in Figures 14 and 15. The phase composition of TCP cement (Figure 14A) is mainly represented by the apatite phase and a smaller amount of brushite and TCP phases, the latter one being an intermediate phase of brushite transformation into HA. The formation of HA is due to  $\text{pH} \approx 7$  of the Ringer solution. Curiously, several literature references dedicated to apatitic cements based on Sr-TCP reported that Sr inhibited apatite formation.<sup>[64–66]</sup>

The XRD pattern of the Sr-TCP cement (Figure 14B) is also represented by broad and less intense apatite reflexes, indicating a decrease in crystallinity due to the Sr incorporation into the lattice. The peak shift towards smaller angles due to Sr substitution was difficult to detect due to the peaks broadening.

According to the SEM data (see Figure 15) for the Sr-containing cement, the crystal size decreased after aging in the Ringer solution (compare A1 and B1 in Figure 15).

The microstructure of the Sr-TCP cement fracture surfaces samples (Figure 15A2,B2) was characterized by smaller and densely packed particles compared to the TCP cement (Figure 15A1,B1), which is consistent with the XRD data described above.

To the best of our knowledge, there are no literature references describing the behavior of brushite cements in model mediums.

### 2.3. Cell Tests

The study of the metabolic activity of fibroblasts of the 3T3 line in the presence of extracts from the investigated cement materials was carried out by means of the MTT test, and the obtained results are shown in Figure 16.

The results of the study showed that powder extracts did not have a noticeable effect on the cell viability, and there were no significant differences between the TCP and Sr-TCP cements.

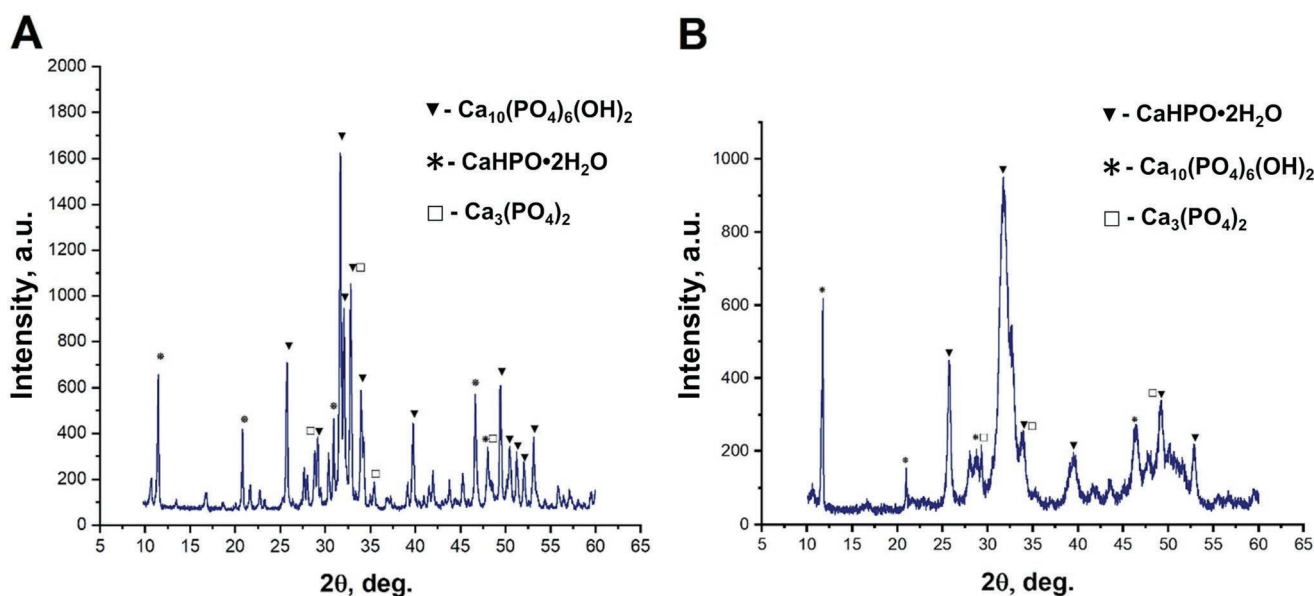


**Figure 14.** XRD patterns of A) TCP cement and B) Sr-TCP cement after soaking in Ringer solution for 21 d.

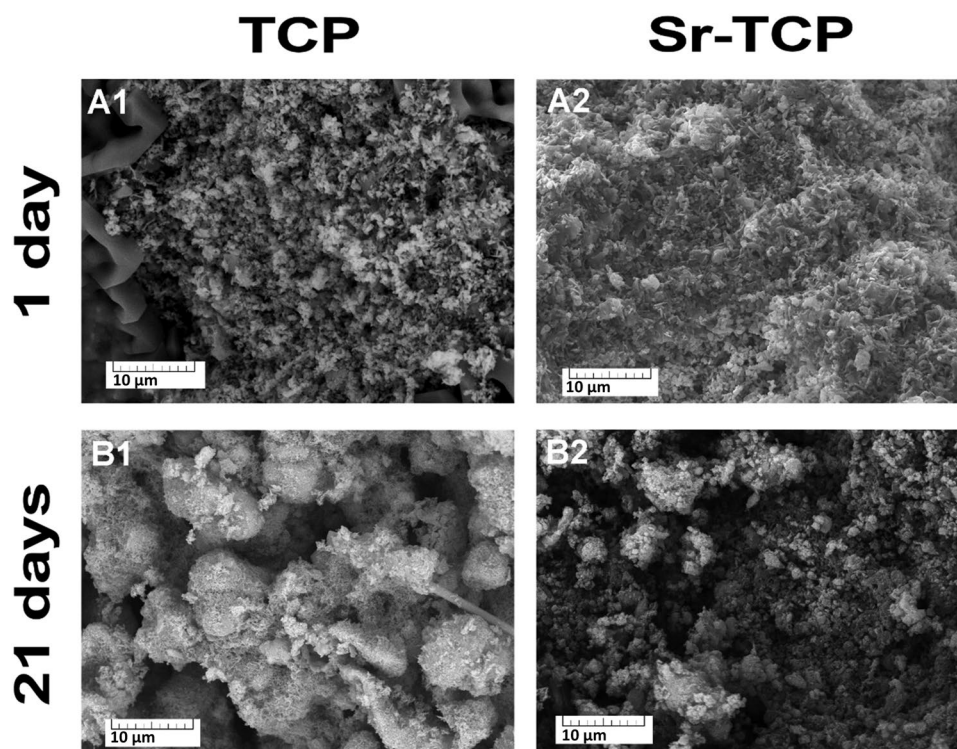


**Figure 15.** SEM microstructure of TCP and Sr-TCP cements after soaking in Ringer solution for 1 and 21 d.

The direct contact method was applied to investigate the adhesion and spreading of DPSC cells on the surface of the cement samples. The results were obtained for 72 h of the DPSC seeding (Figures 17 and 18).

Normal morphology of the DPSC cells was observed on the investigated cement samples, the cells were uniformly distributed and spread out after 72 h (Figure 17). Figure 17A1–C1 demonstrates that the number of cells on the surface of the Sr-TCP sample is higher than on the TCP cement and control sample. Indeed, the cell mass on the Sr-TCP sample is about 30% higher than on the surface of the TCP sample and about

50% higher—than on the control surface (Figure 18). However, for cement samples, 4–6% dead cells are observed.

Based on the results presented in Figures 17 and 18, it can be concluded that the Sr-TCP cement promotes cell proliferation and the increase in the DCPD cell mass. These observations confirm that Sr addition improves cells proliferation.<sup>[67,68]</sup>

### 3. Conclusions

The short-term characterizations, including a fine time-sampling, carried out by time-resolved EDXRD, THz-TDS, and IR Spectroscopy techniques provided the insights into the hardening mechanism of the Sr-TCP cement. The Sr-TCP phase was no longer detectable after 45 min of the process, during this time period an appearance (after 10 min from the beginning) and constant increase of the DCPD phase was detected. It is possible to conclude that during the first time interval, 0–45 min, the Sr-TCP phase underwent a fast disaggregation/re-aggregation and a part of disaggregated particles dissolved and precipitated as the DCPD phase. These results obtained by the EDXRD technique are in good agreement with those collected for the same time period by the THz-TDS, evidencing the max conversion rate of Sr-TCP into DCPD at 45 min. Further confirmation of these results was provided by the FTIR detecting the well-defined DCPD bands at 45 min time point.

After the initial period of hardening, the crystallization and growth of the DPCD phase took place and lasted until 6 h, as detected by the EDXRD, in agreement with the FTIR measurements. The final time period of measurements (6–21 h)—the crystallization/growth process of the DCPD phase—was char-

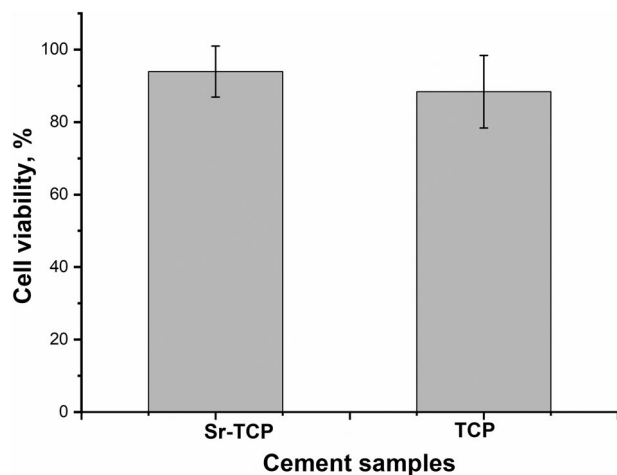


**Figure 16.** MTT test results of the metabolic activity of the 3T3 cells for 24 h incubation with 3 d extracts. Control sample—glass slide—corresponds to 100%. The error bar is mean  $\pm$  SD.

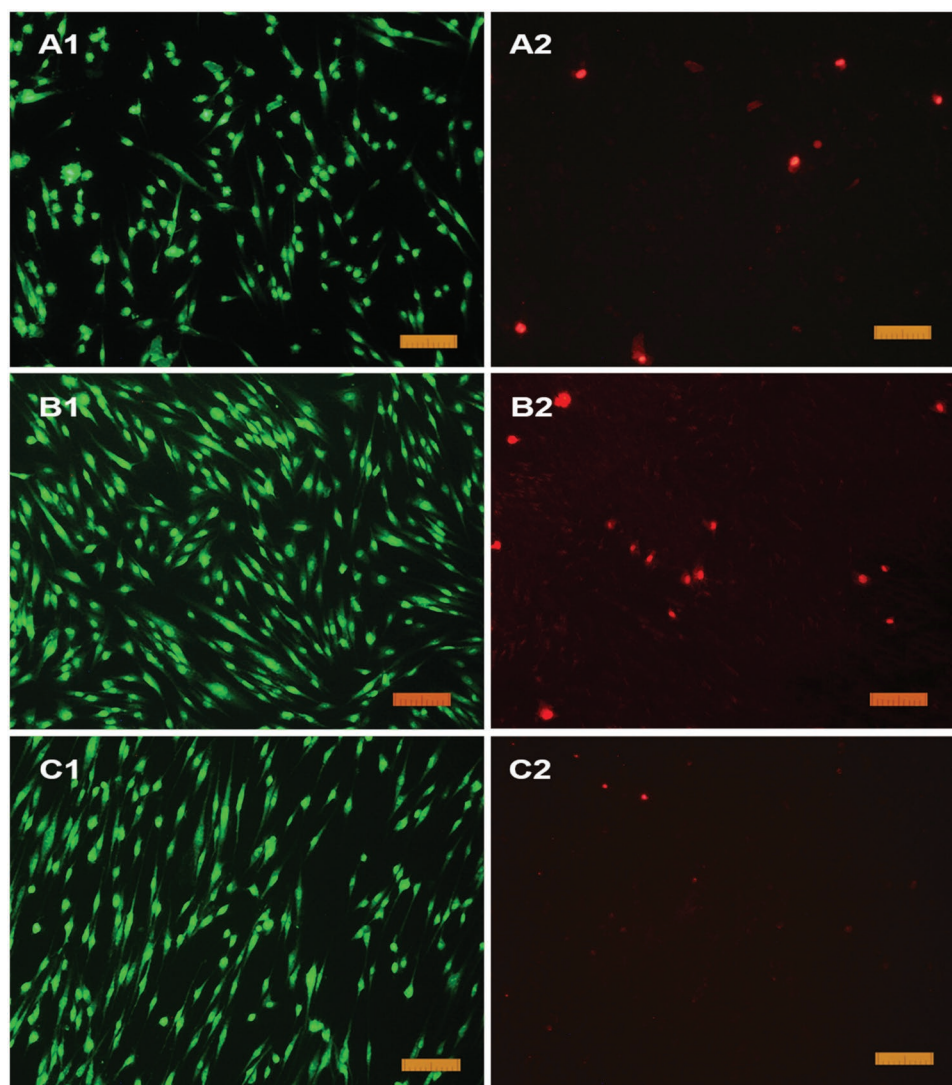


**Figure 17.** DPSC cells cultured for 72 h on the surface of the TCP and Sr-TCP cements: A) TCP cement, B) Sr-TCP cement, C) control. Dyeing SYTO 9 (1) and PI (2) (scale 100  $\mu\text{m}$ ).

acterized by an oscillatory behavior consisting in a fast peaks intensity modulation, as revealed by the short-term EDXRD and confirmed by the long term XRD measurements.

The compressive strength of the Sr-TCP cement increased from 4.5 MPa after 2 h of setting, to 9.6 MPa, after 7 d and reached its maximum at 13.3 MPa after 21 d.

The  $\beta$ -TCP and Sr-TCP cements were soaked in the Ringer solution for 21 d. The phase composition and microstructure of cements transformation took place upon cements soaking. After 21 d, it was represented by the apatite phase and a smaller amount of brushite and TCP phases.

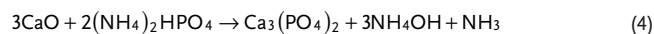
The study of the metabolic activity of fibroblasts of the 3T3 line with extracts from the investigated cements was carried out by means of the MTT test. The obtained results testified that powder extracts did not have a noticeable effect on the cell viability, and there were no significant differences between the TCP and Sr-TCP cements.

The direct contact method was applied to investigate the adhesion and spreading of the human DPSC cells on the

surface of the cement samples. Normal morphology of the DPSC cells was observed: cells were uniformly distributed and spread out after 72 h. The number of cells on the surface of the Sr-TCP sample was higher than on the TCP cement and control sample: the cell mass on the Sr-TCP sample was about 30% higher than on the surface of the TCP sample and about 50% higher—than on the control surface. It can be concluded that the Sr-TCP cement promotes cell proliferation and the increase in the DCPD cell mass. The developed cement is promising for biomedical applications for bone tissue.

#### 4. Experimental Section

*Synthesis of Sr-Substituted  $\beta$ -TCP Powder and Cement Preparation:*  $\beta$ -TCP powder was synthesized according to Equation (4):



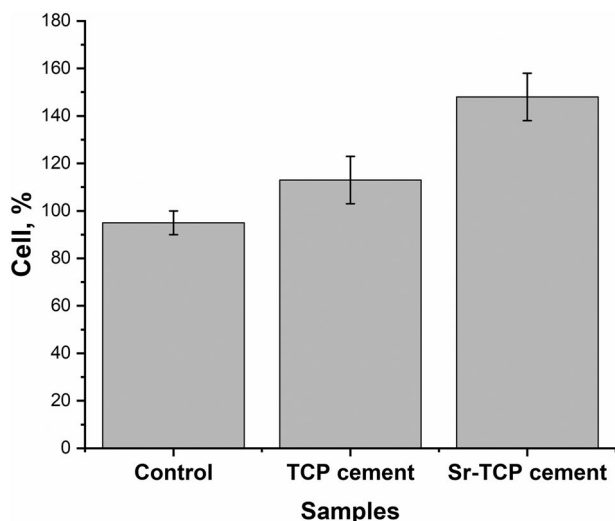
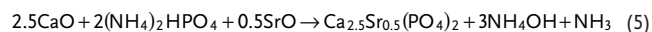


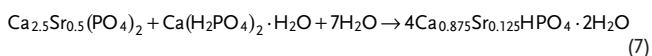
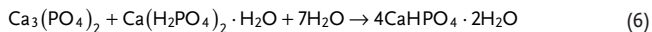
**Figure 18.** DPSC amount on the surface of cement samples after 72 h of seeding: control (glass)—100%, TCP cement, Sr-TCP cement. The error bar is mean  $\pm$  SD.

Sr substituted tricalcium phosphate powder with 13.2 wt% of Sr (Sr- $\beta$ -TCP), which corresponds to the formula  $\text{Ca}_{2.5}\text{Sr}_{0.5}(\text{PO}_4)_2$ , was synthesized by mechanical activation method<sup>[69]</sup> according to the Equation (5):



Freshly calcined at 950 °C powders of SrO (5.2 g, 0.05 mol) and CaO (10 g, 0.18 mol) (chemical grade, Sigma-Aldrich, St. Louise, USA), respectively, and  $(\text{NH}_4)_2\text{HPO}_4$  (26.4 g, 0.2 mol) (chemical grade, Khimmed, Moscow, Russia) were placed in a planetary mill drum with 200 g of zirconium oxide grinding bodies and grounded at a rotation speed of 1500  $\text{min}^{-1}$  for 30 min. After that, 200 mL of distilled water was added to the drum and the grinding was continued for another 30 min. Then the resulting suspension was filtered on a Buchner funnel, washed with water and dried in a drying box at 110 °C for 12 h. The resulting powder was annealed at 400 °C to remove water and ammonia residues.

Cement samples were prepared as described earlier in ref. [14]. Sr-TCP or  $\beta$ -TCP powders amounts calculated according to Equations (6) and (7) were mixed with monocalcium phosphate monohydrate (MCPM) (chemical grade, Sigma-Aldrich, St. Louise, USA) and the resulting powder was mixed with the hardening liquid, containing 8% of citric acid solution (chemical grade, Khimmed, Moscow, Russia). The powder-to-liquid ratio was 4:1. The addition of citric acid allows one to increase the setting time of cement from about 1 min up to about 8 min.<sup>[18]</sup> The set cements were placed in Teflon molds and cement samples were prepared according to the standard GOST R 57953-2017 (Russian Federation).



**Angular Dispersive X-Ray Diffraction (XRD) Analysis:** X-ray powder diffraction analysis of  $\beta$ -TCP and Sr- $\beta$ -TCP powders calcined at 900 °C and cements after 1, 2, 7, and 21 d of setting was performed by means of a Rigaku D/Max2500 diffractometer (Japan, Tokyo) with a rotating anode. The measurements were carried out in the reflection mode (Bragg-Brentano geometry) using  $\text{CuK}\alpha$  radiation (wavelength  $\lambda = 1.54183$  Å). Generator operation parameters were the following: accelerating voltage 45 kV, tube current 250 mA. Qualitative analysis of the obtained

diffraction patterns was carried out using the WinXPOW program and the ICDD PDF-2 database.

**Energy-Dispersive X-Ray Diffraction (EDXRD) measurements:** The intensity of the X-Ray beam elastically scattered by a sample as a function of momentum transfer was represented by a X-ray diffraction pattern. The scattering parameter is named after the momentum transfer amplitude:  $q(E, \theta) = aE\sin\theta$ ,  $E$  being the energy of the electromagnetic radiation,  $2\theta$ —the scattering angle and  $a = \text{constant} = 1.014$  Å  $\text{keV}^{-1}$ . The X-ray white beam can be utilized to do the reciprocal space scan and, specifically, to gather a diffraction pattern, by fixing the angle  $2\theta$  (energy dispersive mode, EDXRD) and performing the reciprocal space scan electronically. The energy scan was carried out using an EG&G high purity germanium solid-state detector with an energy resolution of 1.5–2% in the 20–50 keV energy band. The signal was handled by the Maestro software, which performs the necessary analog to digital conversions when the detector is connected to a PC through the ADCAM hardware. For this experiment,  $2\theta$  angle was kept at 4.6°, and the whole Bremsstrahlung in the energy range of 0–50 KeV was used as the diffraction source.

The cement samples were prepared by an intense mixing of the Sr-TCP pristine powder with the hardening liquid. After about 1 min of mixing, a moldable paste was formed. The paste was placed in the sample holder and positioned in the optical center of the diffractometer. Real-time monitoring of the cement hardening process was accomplished by the collecting one diffraction spectra every 2 min. The duration of the entire experiment was about 21 h.

**Terahertz Time-Domain Spectroscopy (THz-TDS):** One of the most promising applications of THz-TDS is in the nondestructive evaluation of composite materials,<sup>[70–73]</sup> materials combining various consistent components with the physical and chemical properties, significantly different from the properties of individual components. Altering the chemical composition or the morphology of the materials, e.g., by aging, exposition to chemical/physical agents, or by chemical reaction results in a change of the dielectric properties. These properties of media can be successfully monitored through THz-TDS, with the evaluation of dielectric parameters and/or the time-dependent changes in the maximal THz electric field amplitude and its position during the experiment time. A THz time-domain spectroscopy system<sup>[74,75]</sup> was used to the kinetics of the cement transformation upon its setting and hardening process, by analyzing the THz electric waveforms and their temporal evolution. The THz-TDS system works in the transmission mode and its operation is based on photoconductive switches, which generate a broadband THz radiation ranging between 0.2 and 2.5 THz. The scheme is depicted in **Figure 19A** and all the technical details are reported in previous works.<sup>[74,76]</sup> The measurements were carried out under ambient conditions (20–23 °C and 50% of humidity) and using a window of cyclo-olefin Zeonex as a sample holder, being transparent in the THz spectral region.<sup>[77–79]</sup> The THz transmitted electric fields of substrate and sample were collected by placing the empty substrate and the cement sample in the THz focal point with an approximately 1 mm spot diameter (see **Figure 19A,B**).<sup>[74]</sup> The temporal evolution of the hardening process was monitored by acquiring 50 repeated acquisitions of the THz transmitted electric field. Each acquisition lasted around 4 min covering 3 h after the cement preparation. Time-domain data pre- and postprocessing were performed using algorithms in MATLAB (ver. 2016b, MathWorks Inc., Natick, MA, USA).

**Infrared (IR) Spectroscopy:** FTIR/ATR absorption spectra were acquired using a VERTEX 70v FT-IR spectrometer, equipped with a Harrick Pro attenuated total reflection (ATR) module with a single reflection diamond crystal at 45°, and a RT-DLaTGS wide range detector. The measurements were carried out at ambient conditions (20–23 °C and 50% humidity). Continuous ATR spectra were collected to follow the reaction immediately after mixing of cement components until no more changes were observed in the spectra. The IR spectra were acquired in the spectral region from 250 to 4000  $\text{cm}^{-1}$  using 64 scans with the spectral resolution of 2  $\text{cm}^{-1}$ , and a 270 s acquisition time for each spectrum. FTIR/ATR data pre- and postprocessing were performed using OPUS 8.2 and dedicated algorithms for weighted linear combination

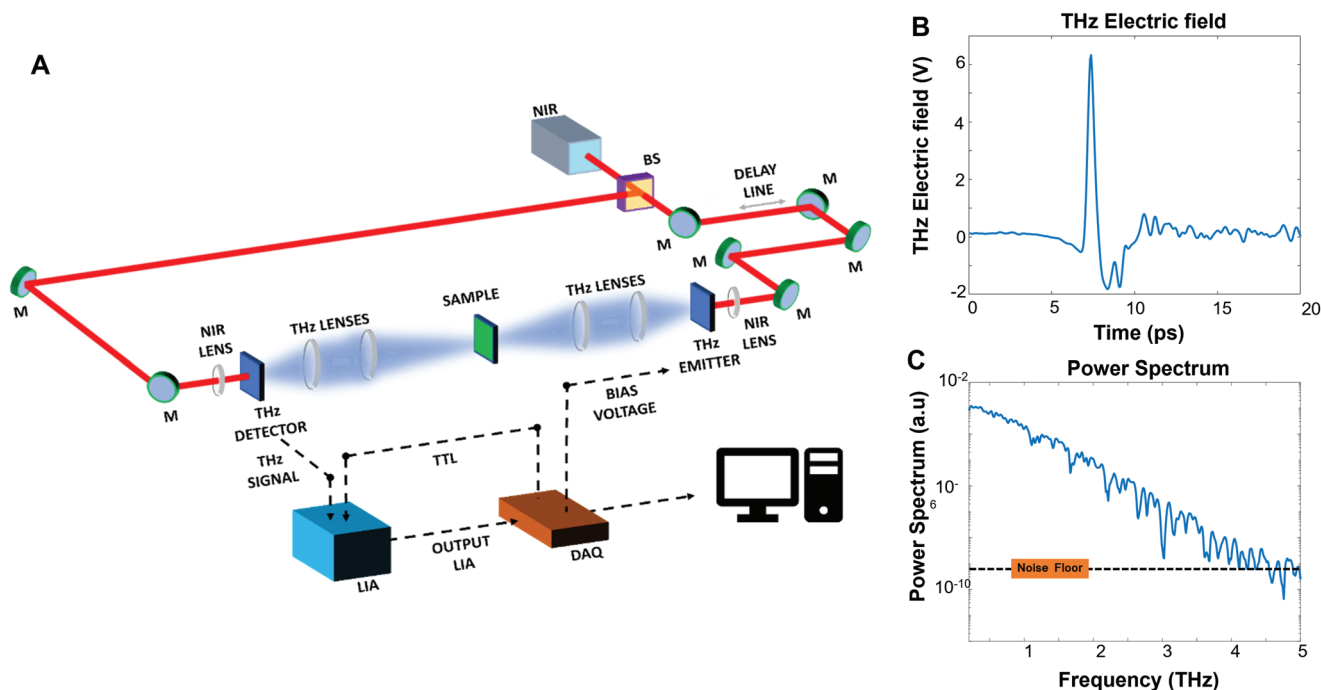


**Figure 19.** A) Schematic layout of THz-TDS setup in transmission mode based on switched photoconductive antennas (PCAs). A femtosecond near-IR (NIR, FemtoFiber NIRpro, Toptica), laser beam is divided into two parts by a beam splitter. The temporal width of the laser is 100 fs and its central wavelength is 780 nm. Its repetition rate is 80 MHz, with an average power of 150 mW. Some mirrors (M) convey the laser beams illuminating twin G10620-11 Hamamatsu photoconductive antennas (PCAs) emitting and collecting THz radiation. The THz emitter and THz detector, where they were focused by a NIR lens. Here the THz beam was produced and detected, respectively. A stack of transparent THz lenses collimated and focused THz radiation along the path and a gas cell was inserted into the THz propagation region. The acquisition chain consisted of a Lock-in amplifier (LIA), a data acquisition card (DAQ) and a personal computer for data collection and analysis. The optical delay line was used to sample the THz pulse in the time domain. B) Temporal profile of THz electric field. C) Power spectrum as a function of THz frequency.

were implemented in MATLAB (ver. 2016b, MathWorks Inc., Natick, MA, USA).

**Scanning Electron Microscopy (SEM):** The microstructure of powders and cement samples was studied using scanning electron microscope Tescan Vega II (Czech Republic, Brno). Sample preparation consisted of spraying gold onto the surface of samples using a rotary pumping spray unit Q150R Plus (Quorum Technologies Ltd., UK).

**Mechanical Tests:** Tests of cement samples for determining the ultimate strength and constructing strain–stress diagrams were carried out using a universal testing machine R-05 (Russia, Ivanovo) equipped with a multi-channel Spider measuring system (USA, Kannapolis). The samples of settled cements were prepared in accordance with the GOST R 57953-2017 after 1, 2, 7, and 21 d of setting.

**Behavior of Cements in Ringer solution:** The behavior of cements in the Ringer solution (Sigma-Aldrich, St. Louise, USA) was studied. For this purpose, 1 g of cement paste after its setting (i.e., about 8 min after mixing of the initial cement powder and hardening liquid) was immersed in a container with 50 mL of the Ringer solution containing a TRIS buffer with a pH of 7.4 and placed in a thermostat at a physiological temperature of 37 °C.

**In Vitro Cell Studies:** Biological studies of cements included an assessment of their possible toxicity (indirect contact of the test culture (extracts from samples) and cytocompatibility (for nontoxic samples, direct contact of the test culture)).

The study of the metabolic activity of a standard NCTC 3T3 fibroblast cell line of mouse subcutaneous connective tissue in the presence of extracts from the investigated cement materials was carried out using the MTT test.

To study the adhesion, spreading of cells and biological compatibility with the investigated cement samples, the direct contact method was used. Cement samples were placed in the wells of a 24-well plate, after

which DPSC cells with a density of 40 000 cm<sup>-2</sup> were seeded on their surface. The fluorescent dye SYTO 9 in the study mode  $\lambda_{\text{ex}} = 450\text{--}490$  nm,  $\lambda_{\text{emiss}} = 515\text{--}565$  nm stains the DNA and RNA of living and dead cells green, which makes it possible not only to visualize cells using a fluorescent microscope, but also to determine the nature of their adhesion and spreading on the surface of the material. The intercalating reagent propidium iodide (PI) in the study mode  $\lambda_{\text{ex}} = 546$  nm,  $\lambda_{\text{emiss}} = 575\text{--}640$  nm stains the nuclei of dead cells red, which makes it possible to identify the percentage of non-viable cells.

The images with cells were obtained using an inverted luminescent microscope Axiovert 200 (Carl Zeiss, Germany), the number of viable cells was calculated on a fixed surface area (on micrographs) as the number of cell nuclei stained with Hoechst 33 342 (all cells) and PI (dead cells).

**Ethics Statement:** The DPSC culture was extracted from the third molars (of a 16 year old donor), which were removed for orthodontic indications at the Central Research Institute of Dentistry and Maxillofacial Surgery of the Ministry of Health in Moscow, Russia, in accordance with an agreement with the Ethics Committee of the Institute of Theoretical and Experimental Biophysics, Russian Academy of Sciences, Puschino, Moscow region, Russia, N 35 on 05/03/2022, after the consent signed by the patient's parents. All experiments, including cells, were carried out in accordance with appropriate clinical practice and ethical principles of the current version of the Helsinki Declaration.

**Statistical Analysis:** Statistical analysis was performed on experimental data related to the investigation of metabolic activity of a standard NCTC 3T3 fibroblast cell line and to the adhesion study on DPSC cells. A set of 24 cement samples were placed on a 24 well plate. Extracts from each well were examined and mean values and the corresponding mean square errors were reported in Figure 17. For adhesion test, dead cell nuclei were stained using the intercalating reagent propidium iodide (PI)

in the study mode  $\lambda_{\text{ex}} = 546 \text{ nm}$ ,  $\lambda_{\text{emiss}} = 575\text{--}640 \text{ nm}$ . Results related to specific cement (TCP and Sr-TCP) were used to calculate mean values and correspondent mean square errors as reported in Figure 18.

## Acknowledgements

The work was partially financially supported by the Russian Science Foundation, grant No. 22-23-00278. Authors are grateful to M.Sc. Pavel Milkin for participation in the energy dispersive X-ray diffraction measurements. The assistance of the technicians Mr. Luca Imperatori and Mr. Marco Ortenzi is gratefully acknowledged.

Open access funding provided by Consiglio Nazionale delle Ricerche within the CRUI-CARE Agreement.

## Conflict of Interest

The authors declare no conflict of interest.

## Author Contributions

Conceptualization: J.V.R. and I.V.F.; data curation: J.V.R., I.V.F., A.A.F., M.F., Ya.Yu.F., A.A., A.D., M.D.F., M.P., S.L., M.DM.DB., V.G.Y.; formal analysis: A.A.F., I.V.A.; funding acquisition, J.V.R., I.V.F.; investigation, I.V.F., A.A.F., G.A.D., M.F., Ya.Yu.F., A.A., A.D., M.D.F., S.L., M.DM.DB., V.I.P.; methodology: J.V.R., I.V.F., G.A.D., M.F., Ya.Yu.F., I.V.A., A.A., M.P., V.I.P., M.B.C.; project administration: J.V.R., resources, J.V.R., I.V.F., G.A.D.; supervision: J.V.R.; validation, J.V.R., I.V.F., G.A.D., I.V.A., V.G.Y., V.I.P., M.B.C.; visualization J.V.R., I.V.F., A.A.F., M.F.; writing—original draft, J.V.R., I.V.F., A.A.F., M.F., A.D., M.D.F., M.P., S.L.; writing—review & editing, J.V.R., A.A.F. All authors have read and agreed to the published version of the manuscript.

## Data Availability Statement

The data that support the findings of this study are available from the corresponding author upon reasonable request.

## Keywords

bone cement, brushite, energy-dispersive X-ray diffraction, strontium doped tricalcium phosphate cement, strontium substituted tricalcium phosphate cement, terahertz spectroscopy

Received: April 12, 2022

Revised: May 23, 2022

Published online: June 27, 2022

- [1] V. Hegde, J. E. Jo, P. Andreopoulou, J. M. Lane, *Osteoporosis Int.* **2016**, *27*, 861.
- [2] P. H. A. Carvalho, L. B. Moura, M. F. Real Gabrielli, M. A. Cabrini Gabrielli, V. Antonio Pereira Filho, *J. Cranio-Maxillofac. Surg.* **2018**, *46*, 1905.
- [3] G. E. Gaski, C. Metzger, T. McCarroll, R. Wessel, J. Adler, A. Cutshall, K. Brown, Y. Vodovotz, T. R. Billiar, T. O. McKinley, *J. Orthop. Trauma* **2019**, *33*, 220.
- [4] Y. Gu, R. Zhuang, X. Xie, Y. Bai, *J. Biomed. Mater. Res., Part B* **2020**, *108*, 1669.
- [5] M. C. Peters, E. Bresciani, T. J. E. Barata, T. C. Fagundes, R. L. Navarro, M. F. L. Navarro, S. H. Dickens, *J. Dent. Res.* **2010**, *89*, 286.
- [6] S. K. Lee, S. K. Lee, S. I. Lee, J. H. Park, J. H. Jang, H. W. Kim, E. C. Kim, *J. Endod.* **2010**, *36*, 1537.
- [7] M. P. Ginebra, E. B. Montufar, in *Biomedical Foams for Tissue Engineering Applications*, (Ed: P. A. Netti), Woodhead Publishing, Cambridge, UK **2014**, p. 281.
- [8] M. P. Ginebra, E. B. Montufar, in *Bone Repair Biomaterials* (Eds: K. M. Pawelec, J. A. Planell), Woodhead Publishing, Cambridge, UK **2019**, pp. 233–271.
- [9] M. Fosca, J. V. Rau, V. Uskoković, *Bioact. Mater.* **2022**, *7*, 341.
- [10] B. Cecen, A. Kalemata, G. Topates, L. D. Kozaci, in *Handbook of Biomaterials Biocompatibility* (Ed: S. Webber), Woodhead Publishing, Cambridge, UK **2020**, pp. 369–393.
- [11] I. Ajaxon, C. Persson, in *The World Scientific Encyclopedia of Nanomedicine and Bioengineering II*, Vol. 3, (Eds: W. Xia, J. Chang), World Scientific, Singapore **2021**, p. 285.
- [12] J. T. Zhang, F. Tancret, J.-M. Bouler, *Mater. Sci. Eng.: C* **2011**, *31*, 740.
- [13] T. Tite, A. C. Popa, L. M. Balescu, I. M. Bogdan, I. Pasuk, J. M. Ferreira, G. E. Stan, *Materials* **2018**, *11*, 2081.
- [14] J. V. Rau, V. M. Wu, V. Graziani, I. V. Fadeeva, A. S. Fomin, M. Fosca, V. Uskoković, *Mater. Sci. Eng.: C* **2017**, *79*, 270.
- [15] J. V. Rau, M. Fosca, V. Graziani, A. A. Egorov, Y.u.V. Zobkov, A. Yu. Fedotov, M. Ortenzi, R. Caminiti, A. E. Baranchikov, V. S. Komlev, *J. Funct. Biomater.* **2016**, *7*, 10.
- [16] V. Graziani, M. Fosca, A. A. Egorov, Y.u.V. Zobkov, A. Yu. Fedotov, A. E. Baranchikov, M. Ortenzi, R. Caminiti, V. S. Komlev, *J. V. Rau, Ceram. Int.* **2016**, *42*, 17310.
- [17] V. Uskoković, V. Graziani, V. M. Wu, I. V. Fadeeva, A. S. Fomin, I. A. Presniakov, M. Fosca, M. Ortenzi, R. Caminiti, J. V. Rau, *Mater. Sci. Eng. C* **2019**, *94*, 798.
- [18] I. V. Fadeeva, M. A. Goldberg, I. I. Preobrazhensky, G. V. Mamin, G. A. Davidova, N. V. Agafonova, M. Fosca, F. Russo, S. M. Barinov, S. Cavalu, J. V. Rau, *J. Mater. Sci.: Mater. Med.* **2021**, *32*, 99.
- [19] D. S. Brauer, N. Karpukhina, G. Kedia, A. Bhat, R. V. Law, I. Radecka, R. G. Hill, *J. R. Soc., Interface* **2013**, *10*, 20120647.
- [20] W. Querido, A. L. Rossi, M. Farina, *Micron* **2016**, *80*, 122.
- [21] A. De Bonis, V. Uskokovic, K. Barbaro, I. V. Fadeeva, M. Curcio, L. Imperatori, R. Teghil, J. V. Rau, *Cell Biol. Toxicol.* **2020**, *36*, 537.
- [22] D. G. Yu, H. F. Ding, Y. Q. Mao, M. Liu, B. Yu, X. Zhao, X. Q. Wang, Y. Li, G. W. Liu, S. B. Nie, S. Liu, Z. A. Zhu, *Acta Pharmacol. Sin.* **2013**, *34*, 393.
- [23] I. Lodoso-Torrecilla, R. K. Gunnewiek, E. C. Grosfeld, R. B. de Vries, P. Habibović, J. A. Jansen, J. J. van den Beucken, *Biomater.* **2020**, *8*, 4792.
- [24] M. Schumacher, M. Gelinsky, *J. Mater. Chem. B* **2015**, *3*, 4626.
- [25] M. Schumacher, A. Lode, A. Helth, M. Gelinsky, *Acta Biomater.* **2013**, *9*, 9547.
- [26] C. Capuccini, P. Torricelli, E. Boanini, M. Gazzano, R. Giardino, *J. Biomed. Mater. Res., Part A* **2009**, *89*, 594.
- [27] S. J. Saint-Jean, C. L. Camire, P. Nevsten, S. Hansen, M. P. Ginebra, *J. Mater. Sci.: Mater. Med.* **2005**, *16*, 993.
- [28] E. Fujihara, M. Kon, K. Asaoka, *Key Eng. Mater.* **2007**, *330*, 795.
- [29] H. Shi, S. Zeng, X. Liu, T. Yu, C. Zhou, *J. Am. Ceram. Soc.* **2018**, *101*, 502.
- [30] M. Dapporto, D. Gardini, A. Tampieri, S. Sprio, *Appl. Sci.* **2021**, *11*, 2075.
- [31] G. Renaudin, P. Laquerrière, Y. Filinchuk, E. Jallot, J. M. Nedelec, *J. Mater. Chem.* **2008**, *18*, 3593.
- [32] X. Wu, Z. Tang, K. Wu, Y. Bai, X. Lin, H. Yang, Q. Yang, Z. Wang, X. Ni, H. Liu, L. Yang, *J. Mater. Chem. B* **2021**, *9*, 5982.
- [33] GDagang, X. Kewei, L. Yaxiong, *J. Mater. Sci.: Mater. Med.* **2010**, *21*, 1927.
- [34] F. S. L. Bobbert, A. A. Zadpoor, *J. Mater. Chem. B* **2017**, *5*, 6175.
- [35] B. Kruppke, A.-S. Wagner, M. Rohnke, C. Heinemann, C. Kreschel, A. Gebbert, H. P. Wiesmann, S. Mazurek, S. Wenisch, T. Hanke, *Mater. Sci. Eng.: C* **2019**, *104*, 109933.

- [36] A. Hanifi, M. H. Fathi, H. M. M. Sadeghi, *J. Mater. Sci.: Mater. Med.* **2010**, *21*, 2601.
- [37] F. Theiss, D. Apelt, B. Brand, A. Kutter, K. Zlinszky, M. Bohner, S. Matter, C. Frei, J. A. Auer, B. von Rechenberg, *Biomaterials* **2005**, *26*, 4383.
- [38] M. Demirel, A. I. Kaya, *J. Mater. Sci.* **2020**, *55*, 6305.
- [39] F. Ozdemir, I. Evans, O. Bretcanu, in *Clinical Applications of Biomaterials*, (Ed: G. Kaur), Springer, Cham, Switzerland **2017**, p. 91.
- [40] E. Boanini, M. Gazzano, C. Nervi, M. R. Chierotti, K. Rubini, R. Gobetto, A. Bigi, *J. Funct. Biomater.* **2019**, *10*, 20.
- [41] M. H. Alkhraisat, C. Moseke, L. Blanco, J. E. Barralet, E. Lopez-Carbacos, U. Gbureck, *Biomaterials* **2008**, *29*, 4691.
- [42] M. H. Alkhraisat, F. T. Mariño, C. R. Rodríguez, L. B. Jerez, E. López-Cabarcos, *Acta Biomater.* **2008**, *4*, 664.
- [43] M. H. Alkhraisat, C. Rueda, J. Cabrejos-Azama, J. Lucas-Aparicio, F. T. Mariño, J. Torres García-Denche, L. B. Jerez, U. Gbureck, E. L. Cabarcos, *Acta Biomater.* **2010**, *6*, 1522.
- [44] S. Tadier, R. Bareille, R. Siadous, O. Marsan, C. Charvillat, S. Cazalbou, J. Amédée, C. Rey, C. Combes, *J. Biomed. Mater. Res., Part B* **2012**, *100*, 378.
- [45] M. Alshaaer, A. S. Afify, M. E. Moustapha, N. Hamad, G. A. Hammouda, F. Rocha, *Clay Miner.* **2020**, *55*, 366.
- [46] A. Taha, M. Akram, Z. Jawad, Z. Alshemary Ammar, R. Hussain, *Mater. Sci. Eng. C* **2017**, *80*, 93.
- [47] S. Pina, J. M. F. Ferreira, *Materials* **2010**, *3*, 519.
- [48] S. Pina, P. M. Torres, F. Goetz-Neunhoeffler, J. Neubauer, J. M. F. Ferreira, *Acta Biomater.* **2010**, *6*, 928.
- [49] S. Pina, P. M. C. Torres, J. M. F. Ferreira, *J. Mater. Sci.: Mater. Med.* **2010**, *21*, 431.
- [50] R. Jayasree, T. S. S. Kumar, R. Venkateswari, R. P. Nankar, M. Doble, *J. Mater. Sci.: Mater. Med.* **2019**, *30*, 113.
- [51] M. Fosca, V. S. Komlev, A. Y. Fedotov, R. Caminiti, J. V. Rau, *ACS Appl. Mater. Interfaces* **2012**, *4*, 6202.
- [52] V. Graziani, M. Fosca, A. A. Egorov, Y. V. Zobkov, A. Y. Fedotov, A. E. Baranchikov, M. Ortenzi, R. Caminiti, V. S. Komlev, J. V. Rau, *Ceram. Interfaces* **2016**, *4*, 17310.
- [53] B. Idowu, G. Cama, S. Deb, L. D. Silvio, *J. Tissue Eng.* **2014**, *5*, 1.
- [54] G. Cama, B. Gharibi, M. Saif Sait, J. C. Knowles, A. Lagazzo, S. Romeed, L. Di Silvio, S. Deb, *J. Mater. Chem. B* **2013**, *1*, 958.
- [55] J. Xu, I. S. Butler, D. F. R. Gilson, *Spectrochim. Acta* **1999**, *55*, 2801.
- [56] V. Uskoković, J. V. Rau, *RSC Adv.* **2017**, *7*, 40517.
- [57] M. P. Ginebra, M. Espanol, Y. Maazouz, V. Bergez, D. Pastorino, *EFORT Open Rev.* **2018**, *3*, 173.
- [58] P. Miranda, E. Saiz, K. Gryn, A. P. Tomsia, *Acta Biomater.* **2006**, *2*, 457.
- [59] S. Kannan, S. Pina, J. M. F. Ferreira, *J. Am. Ceram. Soc.* **2006**, *89*, 3277.
- [60] M. Schumacher, A. Henth, M. Rohnke, M. Gelinsky, *Acta Biomater.* **2013**, *9*, 7536.
- [61] K. Kawabata, T. Yamamoto, A. Kitada, *Phys. B* **2011**, *406*, 890.
- [62] A. Generosi, J. V. Rau, V. S. Komlev, V. Rossi Albertini, A. Yu, Fedotov, S. M., Barinov, *J. Phys. Chem. B* **2010**, *114*, 973.
- [63] E. Şahin, M. Çiftçioğlu, *J. Mater. Chem. B* **2013**, *1*, 2943.
- [64] Z. Yuan, J. Bi, W. Wang, X. Sun, L. Wang, J. Mao, F. Yang, *J. Appl. Biomater. Funct. Mater.* **2021**, *19*, 2280800021996999.
- [65] M. Bohner, H. Tiainen, P. Michel, N. Döbelin, *J. Mater. Sci.: Mater. Med.* **2015**, *26*, 63.
- [66] S. Panzavolta, P. Torricelli, L. Sturba, B. Bracci, R. Giardino, A. Bigi, *J. Biomed. Mater. Res., Part A* **2008**, *84*, 965.
- [67] B. Kruppke, C. Heinemann, A. S. Wagner, J. Farack, S. Wenisch, H.-P. Wiesmann, T. Hanke, *Dev., Growth Differ.* **2019**, *61*, 166.
- [68] Y. Z. Huang, C. G. Wu, H. Q. Xie, Z. Y. Li, A. Silini, O. Parolini, Y. Wu, L. Deng, Y. C. Huang, *Stem Cells Int.* **2019**, *2019*, 4242178.
- [69] N. V. Bulina, M. V. Chaikina, I. Y. Prosanov, D. V. Dudina, *Mater. Sci. Eng.: B* **2020**, *262*, 114719.
- [70] L. Cheng, G. Y. Tian, *J. Sens.* **2012**, *2012*, e408437.
- [71] N. Krumbholz, T. Hochrein, N. Vieweg, T. Hasek, K. Kretschmer, M. Bastian, M. Mikulics, M. Koch, *Polym. Test.* **2009**, *28*, 30.
- [72] R. Bogue, *Assem. Autom.* **2012**, *32*, 211.
- [73] P. Lopato, T. Chady, *Int. J. Appl. Electromagn. Mech.* **2012**, *39*, 427.
- [74] M. Di Fabrizio, A. D'Arco, S. Mou, L. Palumbo, M. Petrarca, S. Lupi, *Appl. Sci.* **2021**, *11*, 562.
- [75] A. D'Arco, M. Di Fabrizio, V. Dolci, A. Marcelli, M. Petrarca, G. Della Ventura, S. L. Lupi, *Biomed. Opt. Express* **2020**, *11*, 1.
- [76] A. D'Arco, M. Di Fabrizio, V. Dolci, M. Petrarca, S. Lupi, *Condens. Matter* **2020**, *5*, 25.
- [77] A. D'Arco, V. Mussi, S. Petrov, S. Tofani, M. Petrarca, R. Beccherelli, D. Dimitrov, V. Marinova, S. L. Lupi, D. C. Zografopoulos, *Nanotechnology* **2020**, *31*, 364006.
- [78] E. V. Fedulova, M. M. Nazarov, A. A. Angeluts, M. S. Kitai, V. I. Sokolov, A. P. Shkurinov, *Proc. SPIE* **2012**, *8337*, 833701.
- [79] S. J. Rezvani, D. Di Gioacchino, S. Tofani, A. D'Arco, C. Ligi, S. Lupi, C. Gatti, M. Cestelli Guidi, A. Marcelli, *Rev. Sci. Instrum.* **2020**, *91*, 075103.